



# Simplify your imaging workflows

**Make research imaging workflows accessible, traceable,  
and secure with Athena Software for Core Imaging Facilities.**

Thermo Scientific™ Athena Software is a premium imaging data management platform designed for core imaging facilities that support materials science research.

Athena Software ensures traceability of images, metadata, and experimental workflows through an intuitive and collaborative web interface.

Find out more at [thermofisher.com/athena](https://thermofisher.com/athena)

**ThermoFisher**  
SCIENTIFIC

# Principles, Functions, and Applications of Optical Meta-Lens

Mu Ku Chen, Yongfeng Wu, Lei Feng, Qingbin Fan, Minghui Lu, Ting Xu,\*  
and Din Ping Tsai\*

A meta-lens is an advanced flat optical device composed of artificial antennas. The amplitude, phase, and polarization of incident light can be engineered to satisfy the application requirements of meta-lenses. Meta-lenses can be designed to achieve a variety of functions, such as diffraction-limited focusing, high focusing efficiency, and aberration correlation, which are useful in various application scenarios. This review focuses on the recent progress in meta-lenses, from fundamentals to applications. The present challenges in this domain are summarized and future prospects are offered. The primary aim of this review is to provide the reader with a comprehensive understanding of meta-lenses and potential inspiration for designing high-performance meta-lenses for feasible applications.

## 1. Introduction

Metasurface technology is an advanced topic in flat optics that has attracted attention in recent years. The fundamental principles, design, fabrication, and applications of metasurfaces have been extensively studied. The artificial antenna array of metasurfaces is used to manipulate the optical responses, such as the amplitude, phase, and polarization of electromagnetic waves. In addition to possessing these unique control capabilities, metasurfaces have the advantage of being flat, ultrathin, lightweight,

and compact. Many applications have been developed based on photonics, for example, beam steering,<sup>[1,2]</sup> meta-holography,<sup>[3–5]</sup> polarization control and analysis,<sup>[6–9]</sup> nonlinear generation,<sup>[10–13]</sup> lasers,<sup>[14]</sup> color displays,<sup>[15]</sup> tunable meta-devices,<sup>[16,17]</sup> meta-lenses, and other novel meta-devices. This review focuses on the recent progress in meta-lenses, and is organized as illustrated in **Figure 1**. First, a brief introduction to the fundamental physics of meta-lenses is presented. Meta-lenses can be categorized into two types according to their material composition: plasmonic meta-lenses and dielectric meta-lenses, and their underlying

mechanisms are discussed. Then, we introduce the key criteria to evaluate and optimize the functionalities of meta-lenses, including focusing efficiency, numerical aperture (N.A.), aberration correction, and tunability. The versatile applications of meta-lenses are demonstrated in polarization imaging systems, phase imaging systems, light-field cameras, and other multifunctional applications. We conclude the review with a discussion on the present challenges in this domain and offer our perspective on the future work. We aim to provide a comprehensive understanding of meta-lenses and their practical applications. We also seek to provide inspiration to the reader with regard to the design of high-performance meta-lenses.

## 2. Principles

### 2.1. Plasmonic Meta-Lenses

At the end of the last century, extraordinary zero-order transmission spectra were observed during the exploration of the optical properties of subwavelength metallic apertures.<sup>[18]</sup> This discovery has inspired extensive research in plasmonics. As one of the most common and practical plasmonic devices, plasmonic flat lenses have attracted considerable attention owing to their ability to exhibit technical advantages that are not available in conventional optics.

#### 2.1.1. Nanoslit-Based Meta-Lenses

Plasmonic nanoslits are typical metal–insulator–metal (MIM) waveguide structures, wherein the electromagnetic energy is transmitted as surface plasmon polaritons (SPPs). **Figure 2a** depicts that phase retardation can be introduced by varying the SPP propagation constants in the waveguide, that is, through

Dr. M. K. Chen, Dr. Y. Wu, Prof. D. P. Tsai  
State Key Laboratory of Ultra-precision Machining Technology  
Department of Industrial and Systems Engineering  
The Hong Kong Polytechnic University  
Hong Kong 999077, China  
E-mail: dinping.tsai@polyu.edu.hk

Dr. M. K. Chen, Dr. Y. Wu, Prof. D. P. Tsai  
Department of Electronic and Information Engineering  
The Hong Kong Polytechnic University  
Hong Kong 999077, China

Dr. L. Feng, Dr. Q. Fan, Prof. M. Lu, Prof. T. Xu  
National Laboratory of Solid-State Microstructures  
College of Engineering and Applied Sciences and Collaborative  
Innovation Center of Advanced Microstructures  
Nanjing University  
Nanjing 210093, China  
E-mail: xuting@nju.edu.cn

 The ORCID identification number(s) for the author(s) of this article can be found under <https://doi.org/10.1002/adom.202001414>.

© 2021 The Authors. Advanced Optical Materials published by Wiley-VCH GmbH. This is an open access article under the terms of the Creative Commons Attribution-NonCommercial-NoDerivs License, which permits use and distribution in any medium, provided the original work is properly cited, the use is non-commercial and no modifications or adaptations are made.

DOI: 10.1002/adom.202001414

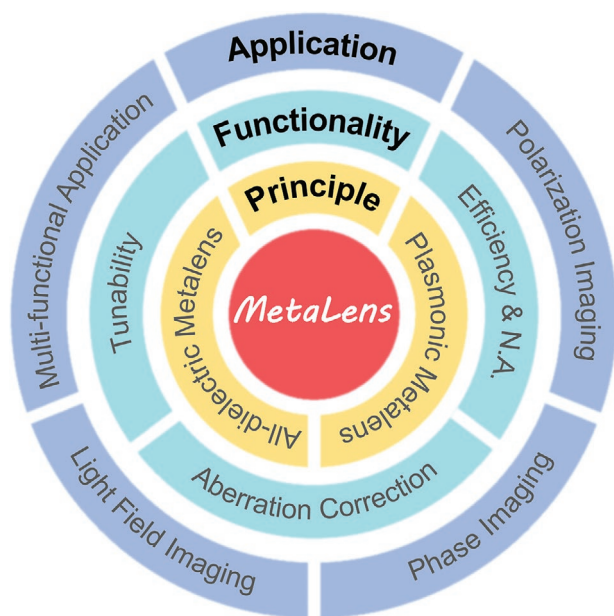


Figure 1. Schematic showing the organization of topics in this review.

propagation phase modulation. The propagation constant can be obtained by solving Maxwell's equations with appropriate boundary conditions:<sup>[19]</sup>

$$\tanh(w\sqrt{\beta^2 - \epsilon_d k_0^2}/2) = -\frac{\epsilon_d \sqrt{\beta^2 - \epsilon_m k_0^2}}{\epsilon_m \sqrt{\beta^2 - \epsilon_d k_0^2}} \quad (1)$$

where  $\beta$  is the SPP propagation constant,  $k_0$  is the optical wave vector in free space,  $w$  and  $h$  are the nanoslit width and thickness, respectively, and  $\epsilon_d$  and  $\epsilon_m$  are the dielectric and metal related dielectric constants, respectively.  $\beta$  can be directly altered by varying  $w$  or  $h$ . The phase retardation,  $\Phi$ , is defined as

$$\begin{aligned} \Phi &= \beta d + \alpha \\ &= \text{Re}(\beta d) + \arg \left[ 1 - \left( \frac{1 - \beta/k_0}{1 + \beta/k_0} \right)^2 \right] \exp(i2\beta d) \end{aligned} \quad (2)$$

where  $\alpha$  is the factor generated from multiple SPP reflections between the entrance and exit interfaces.<sup>[20]</sup>

Based on this concept, several plasmonic flat lenses have been demonstrated in the visible region.<sup>[21–27]</sup> For example, Sun et al.<sup>[24]</sup> theoretically demonstrated beam shaping using a nanoslit array formed on a metal film layer, where the

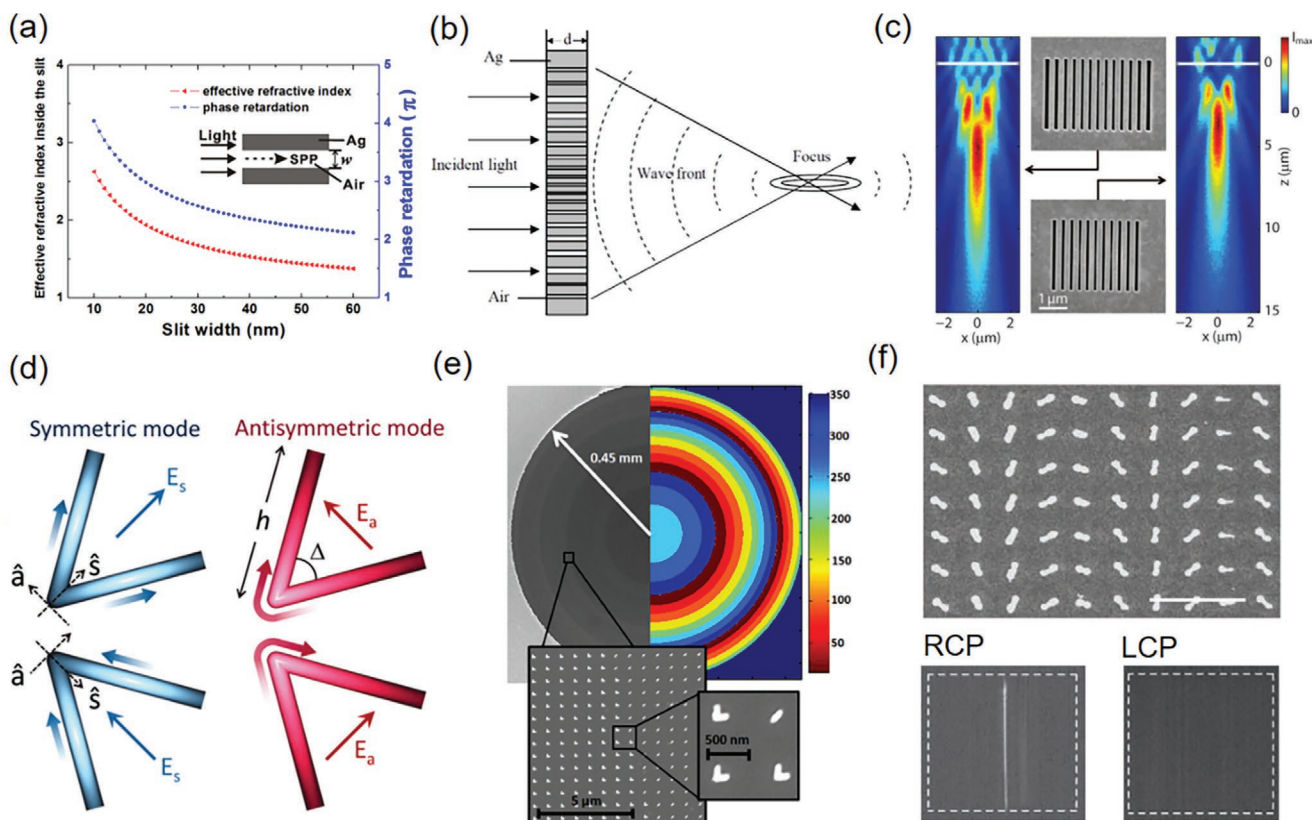


Figure 2. Plasmonic meta-lens: a) The dependence of propagation constant on slit width; inset: surface plasmon polaritons (SPPs) propagating along the slits. Reproduced with permission.<sup>[26]</sup> Copyright 2008, Optical Society of America. b) Slit-based meta-lens. Reproduced with permission.<sup>[25]</sup> Copyright 2005, Optical Society of America. c) Slit-based meta-lens comprising of a 400 nm thick gold film with slit widths ranging from 80–150 nm. Reproduced with permission.<sup>[27]</sup> Copyright 2009, American Chemical Society. d) V-shaped antennas with symmetric and antisymmetric modes. Reproduced with permission.<sup>[31]</sup> Copyright 2011, American Association for the Advancement of Science. e) Antenna-based meta-lens. Reproduced with permission.<sup>[36]</sup> Copyright 2012, American Chemical Society. f) Plasmonic meta-lens scanning electron microscopy (SEM) image (top) and optical microscope images at virtual focal plane (bottom). Reproduced with permission.<sup>[43]</sup> Copyright 2012, Springer Nature.

slit thickness controls the phase retardation. Shi et al.<sup>[25]</sup> theoretically demonstrated that a flat lens based on phase control can be achieved using nanoslits of varying widths (Figure 2b). Xu et al.<sup>[26]</sup> demonstrated that a nanoslit array can implement subwavelength imaging. Fan et al.<sup>[27]</sup> experimentally demonstrated a flat lens based on nanoslit arrays in a gold film (Figure 2c). The flat lens comprised a 400 nm thick metallic film with 80–150 nm slit widths; however, the phase coverage was only  $\approx 0.6\pi$  under 637 nm wavelength laser diode illumination. They also numerically demonstrated that an aperiodic gold slit waveguide array can focus an incident light beam onto a spot as small as  $\lambda/100$ .<sup>[28]</sup> However, it is difficult to achieve full control of the wavefront with plasmonic nanoslit-based meta-lenses due to insufficient phase coverage, low photon throughput, and challenges in the fabrication of intricate designs.

### 2.1.2. Antenna-Based Meta-Lenses

At the surface of a metallic nanoantenna, light waves can be scattered by the collective oscillation of free electrons, and this phenomenon is known as localized surface plasmon resonance (LSPR). LSPR is an electronic-electromagnetic interaction, which can be described using a simple oscillator model that involves radiative and internal damping. Assume that an ideal point charge  $q$  located at a position  $x(t)$  with a spring mass  $m$  and a spring coefficient of  $\kappa$ , is driven through an input electric field with harmonic frequency  $\omega$ .<sup>[29]</sup> Then, the charge experiences internal damping with a damping factor  $\Gamma_a$ ,

$$m \frac{d^2 x}{dt^2} + \Gamma_a \frac{dx}{dt} + \kappa x = q E_0 e^{i\omega t} + \Gamma_s \frac{d^3 x}{dt^3} \quad (3)$$

The internal damping force is proportional to the first derivative  $\frac{dx}{dt}$ , and the charge simultaneously experiences an additional force  $\Gamma_s \frac{d^3 x}{dt^3}$  due to the radiation reaction, known as the Abraham–Lorentz force.<sup>[30]</sup> Assuming a simple harmonic motion  $x(\omega, t) = x_0 e^{i\omega t}$ , the steady-state solution for Equation (3) can be expressed as

$$x(\omega, t) = \frac{\left(\frac{q}{m}\right) E_0}{(\omega_0^2 - \omega^2) + i \frac{\omega}{m} (\Gamma_a + \omega^2 \Gamma_s)} e^{i\omega t} = x_0(\omega) e^{i\omega t} \quad (4)$$

where  $x_0(\omega)$  describes the electromagnetic response of the oscillator, and  $\omega_0 = \sqrt{\kappa/m}$ . Equation (4) implies that the scattering phase modulation range cannot exceed  $\pi$  if a single nanoantenna resonance is involved.

In contrast to nanoslit arrays, antenna-based plasmonic metasurfaces are significantly advanced because they are ultrathin (much less than the wavelength) and simple to fabricate. However, they are still unsuitable for complete wavefront manipulation. Expanding the phase-shift modulation range to  $2\pi$  is an important goal for a high-efficiency transmissive meta-lens.

Yu et al.<sup>[31]</sup> proposed the generalized laws for reflection and refraction in metasurface and demonstrated that the interfacial phase gradient can arbitrarily manipulate transmitted light beams. Thus, a V-shaped nanoantenna array with suitable geometry and orientation can provide  $2\pi$  phase coverage due to symmetric and antisymmetric plasmonic modes (Figure 2d). Such a metasurface can be regarded as a hybrid device generated from the combined modulation of the geometric phase (Pancharatnam Berry phase) and resonant phase.<sup>[32–35]</sup> Four V-shaped antennas with different dimensions are selected to provide each  $\pi/4$  resonant phase shift, and these antennas are rotated by  $90^\circ$  to provide a  $\pi$  geometric phase shift for cross-polarized scattered light. Thus, a set of eight antennas with  $2\pi$  phase coverage was created from the four initial antennas. Based on this strategy, planar lenses free from spherical aberration were demonstrated at  $\lambda = 1.55 \mu\text{m}$  using V-shaped antennas<sup>[36]</sup> (Figure 2e). Thereafter, flat lenses comprising V apertures were demonstrated in the visible region using Babinet's principle.<sup>[37]</sup>

Another method to implement full phase coverage is to modulate the geometric phase.<sup>[4,38–43]</sup> Recent developments in geometric phase metasurfaces have been inspired mainly by the Hasman group's early work.<sup>[44–46]</sup> They experimentally demonstrated that a subwavelength grating could be used to implement a polarization-dependent flat lens at a wavelength of  $10.6 \mu\text{m}$ . Geometry phase modulation is independent of the dimensions of the unit cells, structural resonance modes, and inherent material properties. The Jones matrix can be used to describe the geometric phase modulation. In general, an anisotropic unit cell with a space-varying fast axis can be expressed as

$$T = R(-\theta) \begin{bmatrix} t_x & 0 \\ 0 & t_y \end{bmatrix} R(\theta) \quad (5)$$

where the unit cell imposes complex amplitude  $t_x$  and  $t_y$  on the incident light, which is linearly polarized along the two principal axes that are rotated by  $\theta$  relative to the reference coordinate system, and  $R(\theta)$  is a rotation matrix. When circularly polarized light passes through the nanostructure, the Jones matrix for the transmitted electric field<sup>[42]</sup> can be described as

$$\begin{bmatrix} E_x \\ E_y \end{bmatrix} = \frac{t_x + t_y}{2} \begin{bmatrix} 1 \\ \pm i \end{bmatrix} + \frac{t_x - t_y}{2} \exp(\pm i2\theta) \begin{bmatrix} 1 \\ \mp i \end{bmatrix} \quad (6)$$

The output of the optical fields comprises two orthogonal circular polarizations. The first term implies that the output circular polarization has the same handedness as the incident light without additional phase retardation, and the second term implies that the output circular polarization has opposite handedness with an additional geometric phase  $\pm i2\theta$ , where + and – denote left and right circularly polarized incident light, respectively. Therefore, the geometric phase can cover the entire  $2\pi$  range if the anisotropic nanostructure is rotated from  $0^\circ$  to  $180^\circ$ . In this method, all nanostructures have identical dimensions, resulting in uniform amplitude and specific phase shifts of the transmitted light. To realize a high polarization conversion efficiency and high-purity geometric phase, it is generally

desirable to select perfect subwavelength half-waveplates to compose the unit cells.

Plasmonic planar lenses based on geometry phase modulation have been theoretically and experimentally demonstrated using U-shaped apertures<sup>[42]</sup> and rectangular nano-antennas,<sup>[43]</sup> respectively. Figure 2f depicts the experimental results of the dual-polarity operating plasmonic meta-lens, which is designed based on the geometric phase at visible frequencies.<sup>[43]</sup> However, the focusing efficiency still needs improvement. Sun et al.<sup>[1,5,47]</sup> experimentally demonstrated that reflection arrays comprising plasmonic antennas and a metallic mirror separated by a dielectric spacer exhibit anomalous reflection with high efficiency, and hence improve the manipulation efficiency of a metasurface. Highly efficient reflective flat lenses have also been demonstrated using this approach in near-infrared<sup>[48,49]</sup> and mid-IR regions.<sup>[50]</sup> Recently, Luo et al.<sup>[51,52]</sup> proposed a flat lens consisting of catenary structures that yield continuous geometric phases. Because of the elimination of the resonance effect in discrete unit cells, the efficiency of the catenary-based device is close to the theoretical boundary (25%) of a monolayer plasmonic metasurface. Although plasmonic metasurfaces have shown significant progress, their fundamental efficiency limitations in transmission remain an insurmountable obstacle for practical applications.

## 2.2. Dielectric Meta-Lenses

Huygens' metasurfaces were introduced by Pfeiffer et al. to tune impedances and improve the efficiency of wavefront manipulation.<sup>[53,54]</sup> Total reflection elimination can be achieved by simultaneously exciting electric and magnetic dipole resonances of equal magnitude. Although several devices based on this principle have been successfully demonstrated previously for lower frequencies, the devices operating in the near-infrared or visible light region face many challenges due to material loss and

manufacturing difficulties. Dielectric Huygens' metasurfaces have been proposed to allow spectrally overlapped electric and magnetic dipole moments to overcome material losses.<sup>[55]</sup> Complete  $2\pi$  phase coverage can be accomplished by tailoring the structural dimensions.

Zhang et al.<sup>[56]</sup> experimentally demonstrated that Huygens meta-lenses can achieve diffraction-limited focusing and imaging in the transmissive mode (Figure 3a), with a building block thickness of  $\approx 1/8$  of the free-space wavelength and a focusing efficiency of up to 75% for linearly polarized light. However, several factors hinder practical development. The Huygens' metasurface only achieves full  $2\pi$  phase coverage within a relatively narrow bandwidth, and there is considerable resonance mode coupling between adjacent nanostructures, which significantly degrades the performance of the meta-lens at high N.A. owing to the large phase gradient near the edges.<sup>[57]</sup>

High-contrast transmission arrays (HCTAs) or high-contrast reflection arrays are important<sup>[58–64]</sup> to overcome the disadvantages of Huygens' metasurfaces, while maintaining sufficient wavefront manipulation. The structural characteristics of HCTAs are analogous to blazed-binary diffractive elements, and this was proposed at the end of the last century.<sup>[65–67]</sup> In general, HCTAs comprise high-index unit cells resting on a low-index substrate,<sup>[58]</sup> with a building block thickness comparable to the targeted wavelength (i.e.,  $0.5\text{--}1.0\lambda$ ). The dielectric unit cells can be considered as truncated waveguides that confine the optical wave inside subwavelength structures with negligible material absorption, which behave as a group of resonators with weakly coupled low-quality factors.<sup>[68]</sup> Fabry–Perot effects are inevitable due to the impedance mismatch at the end of the waveguide. Therefore, the propagation phase arises from the superposition of coupling, radiation, and propagation modes. All these effects can be estimated by using a rigorous electromagnetic simulation. Khorasaninejad et al.<sup>[69]</sup> demonstrated that waveguiding is the dominant physical mechanism for the realization of the propagation phase. For a single waveguide, the propagation

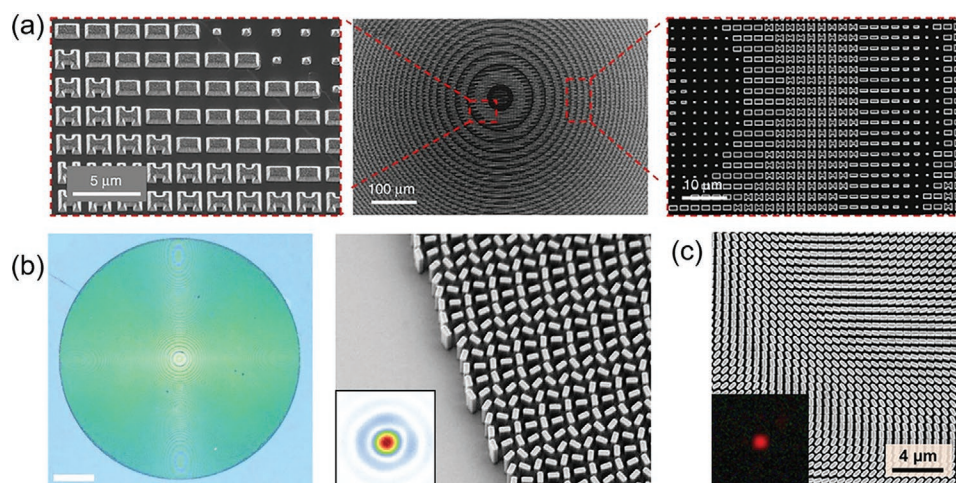


**Figure 3.** Dielectric meta-lens: a) SEMs of the top view of a fabricated mid-infrared Huygens meta-lens. Reproduced with permission.<sup>[56]</sup> Copyright 2018, Springer Nature. b)  $\text{TiO}_2$  based meta-lens digital image (left) and SEM image (right); inset: measured intensity distribution at 532 nm. Reproduced with permission.<sup>[78]</sup> Copyright 2016, American Association for the Advancement of Science. c) GaN-based meta-lens SEM; inset: measured intensity distribution at 633 nm. Reproduced with permission.<sup>[79]</sup> Copyright 2017, American Chemical Society.

phase  $\varphi_{\text{wg}}$  of an optical wave passing through a unit cell of height  $H$  is defined as

$$\varphi_{\text{wg}} = \frac{2\pi}{\lambda} n_{\text{eff}} H \quad (7)$$

where  $\lambda$  is the free-space wavelength, and  $n_{\text{eff}}$  is the effective index, which can be tailored by altering the structural dimensions, for example, nanopillar width  $W$  and height  $H$ . To achieve  $\Delta \varphi_{\text{wg}} = 2\pi$  phase coverage between unit cells with maximum and minimum filling factors, the following condition should be satisfied.

$$H = \frac{\lambda}{\Delta n_{\text{eff}}} \quad (8)$$

where  $\Delta n_{\text{eff}} = n - 1$ , and  $n$  is the refractive index of the dielectric material. A dielectric material with a refractive index larger than 2, that is,  $\Delta n_{\text{eff}} > 1$ , can obtain  $2\pi$  phase coverage with sub-wavelength height.

The array period  $P$  must be small enough to satisfy the Nyquist sampling criterion,

$$P < \frac{\lambda}{2\text{N.A.}} \quad (9)$$

for the chosen N.A. and operating wavelength. Therefore, the fabrication of a high-frequency or large N.A. meta-lens becomes more challenging. The maximum filling factor and the minimum feature of the unit cell design are limited by the critical constraints of fabrication. Satisfying Equation (9) only ensures that the metasurface can yield an accurate phase shift for each array position but does not eliminate the possibility of higher-order diffraction, particularly for meta-lenses with low N.A.

Silicon is the preferred material for NIR dielectric metasurfaces owing to its many advantages, including high refractive index, low absorption loss, and mature fabrication technology.<sup>[68,70–74]</sup> A silicon-based meta-lens in transmission mode that could achieve high efficiency and near diffraction-limited focusing was proposed by Arbabi et al.<sup>[68]</sup> The focusing efficiency decays with the increment of N.A. due to the reduced phase levels at the metasurface edge. Silicon-based meta-lenses are also realized in mid-IR and long-wavelength IR regions<sup>[75–77]</sup> with similar performance. However, the performance degrades rapidly for visible light owing to optical absorption loss, particularly for short operating wavelengths ( $\lambda < 500$  nm).

In the visible light region, many types of dielectric materials can be used as materials for designing meta-lenses, including gallium nitride (GaN), silicon nitride ( $\text{Si}_3\text{N}_4$ ), and titanium dioxide ( $\text{TiO}_2$ ). These materials have refractive indices ranging from 2.0 to 2.5. Hence, the nanostructure design aspect ratio must be sufficiently high to achieve full wavefront manipulation. Khorasaninejad et al.<sup>[78]</sup> demonstrated a high-aspect-ratio  $\text{TiO}_2$  meta-lens with a large N.A., and the efficiencies are up to 86%, 73%, and 66% at 405 nm, 532 nm, and 660 nm of wavelength, respectively. The meta-lens was fabricated by electron-beam lithography and atomic layer deposition, as depicted in Figure 3b. The high efficiency GaN-based meta-lenses operating in the visible region were also utilized for multiplexed color

routing, as depicted in Figure 3c.<sup>[79]</sup> This work showed excellent compatibility with semiconductor fabrication processes. The polarization-dependent optical response of the metasurface is related to the anisotropic cross-section of the nanopillars of the metasurface. This unique optical response is attributed to the different effective refractive indices for the propagation modes polarized along the principal axes of the nanopillars. Many polarization-dependent meta-lenses have been demonstrated.<sup>[77,80,81]</sup> These meta-lenses have provided a good foundation for developing multi-functional photonic devices.

### 3. Functionalities

Focusing efficiency is commonly used to characterize the focusing ability of the meta-lens, and is defined as the ratio of optical power from the corresponding focused beam to that from the incident beam. High focusing efficiency results from the accurate manipulation of the phase and amplitude of the incident light beam. In principle, an ideal meta-lens acts as a perfect transformation optical device to control and focus all the incident light to the designated spatial position with the least loss. The light ray tailoring requirements of the incident light waves are determined by the diameter of the lens and the focal length. These two conditions are used to determine the N.A. of the lens. The N.A. is one of the important specifications of a conventional optical lens. N.A. is one of the parameters or specifications that is set for the design of metastructures of the meta-lens.

The nanoantennas act as the meta-atom, and the secondary light source at the metasurface typically resonates at a fixed frequency with a sharp bandwidth. This intrinsic property of the meta-lens is the primary reason for the chromatic aberration during focusing. For single-wavelength meta-lens focusing and imaging, the design of the meta-lens is relatively simple. However, for full-color wide-band imaging in the visible wavelength range of 400–700 nm, accurate achromatic focusing along with diffraction limit spatial resolution is required. To achieve this, an integrated resonant unit (IRU) and the differential phase (DP) equation were introduced by Hsiao et al.<sup>[97,98]</sup> IRU is a building block with multiple resonators, and its functionality is determined by tuning the multiple resonances. The IRU library can provide a series of linear and smooth phase compensations to engineer the phase distribution in the continuous working band of the wavelength. The DP equation is derived from the phase equation of the focusing lens. It is used to determine the additional phase requirement for a specific working band of the wavelength under the same focal length condition. The phase compensation can be fulfilled by IRUs to realize the achromatic focusing of the meta-lens. These design principles are used to accomplish and realize the full-color wide-band achromatic meta-lens for focusing and imaging in the visible wavelength region. The imaging quality can be evaluated in terms of the contrast, modulation transfer function, spatial resolution, etc.

Tunable meta-lenses are in high demand. Tunability can be achieved in many ways, either inherently or externally. These aspects of the functionalities of the meta-lenses are discussed in detail in the following sections.

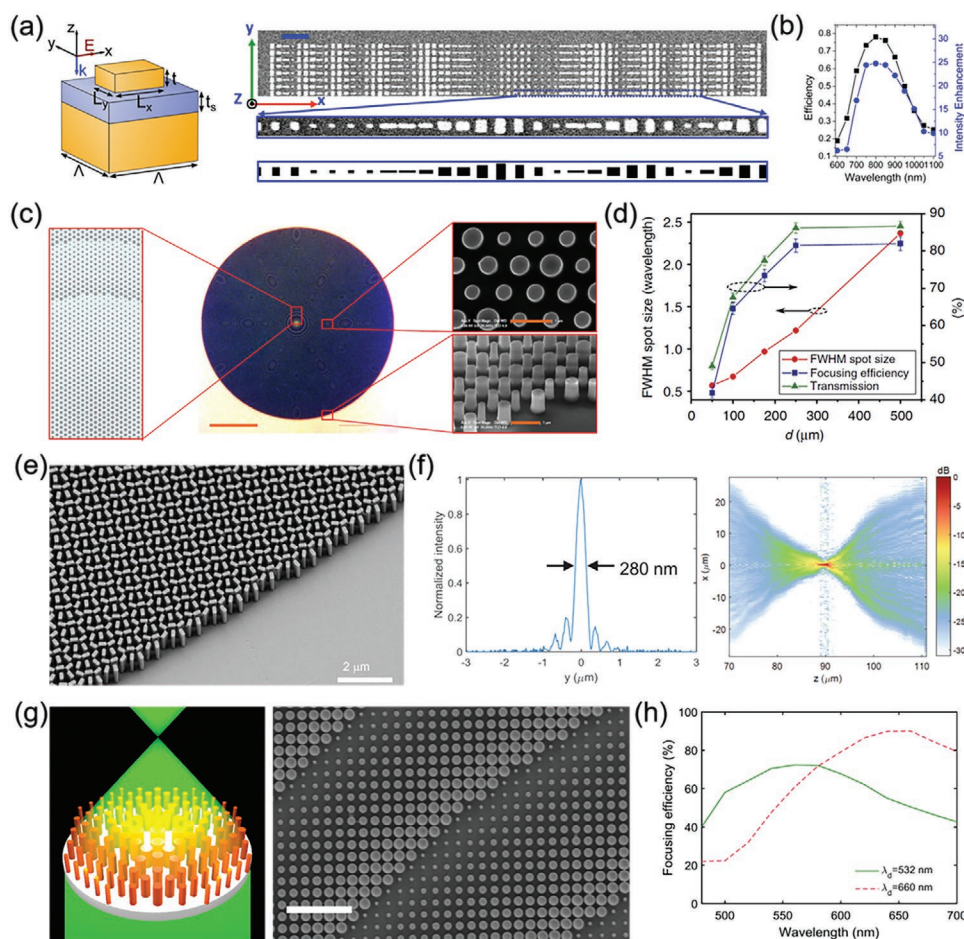


**Figure 4.** High efficiency imaging: a) Schematic of a gold-glass-gold unit cell, and SEM image (bar length is 1  $\mu\text{m}$ ) of a portion of the gold nanobricks designed for the wavelength of 800 nm.<sup>[49]</sup> b) Focusing efficiency and intensity enhancement. Reproduced with permission.<sup>[49]</sup> Copyright 2013, American Chemical Society. c) Aperiodic high-contrast transmission array (HCTA), fabricated HCTA lens optical microscope, and SEM images;<sup>[68]</sup> d) measured full width half maximum (FWHM) of spot size at focal plane, and transmission and focusing efficiency for HCTA micro-lenses with respect to focusing distance. Reproduced with permission.<sup>[68]</sup> Copyright 2015, Springer Nature. e) SEM micrographs of the tilted edge view of the fabricated meta-lens;<sup>[78]</sup> f) corresponding vertical cuts in the focal spots of the meta-lens at 405 nm having FWHM = 280 nm. Reproduced with permission.<sup>[78]</sup> Copyright 2016, American Association for the Advancement of Science. g) Meta-lens operating in transmission mode and SEM image of top view of meta-lens edge;<sup>[69]</sup> h) measured focusing efficiency with respect to wavelength for meta-lenses with designed wavelengths = 532 and 660 nm with N.A. = 0.6. Reproduced with permission.<sup>[69]</sup> Copyright 2016, American Chemical Society.

### 3.1. Focusing Efficiency and Numerical Aperture

The efficiency of the meta-lens is key to the applications of imaging and sensing. The efficiency of the meta-lens can be improved by suppressing i) scattering caused by the structures with wavelength scale dimensions, ii) reflection caused by an impedance mismatch, and iii) material absorption caused by material loss. The resonance, geometric, and propagation phase mechanisms can be used to enhance the focusing performance. Pors et al.<sup>[49]</sup> achieved broadband focusing by a reflective meta-lens using MIM configuration and plasmonic resonance phase modulation, as shown in Figure 4a. Eight different elements provide a hyperboloidal phase profile, which can be modulated along one desired dimension by varying both the lateral dimensions of the nanobricks. Consequently, the flat mirror can focus linearly polarized light with 78% efficiency at a wavelength of 800 nm, as shown in Figure 4b. However, the

focusing efficiency of the reflective meta-lens is limited by the interacting reflection area in this case.

Faraon et al. showed a transmissive meta-lens with HCTA flat diffractive elements operating at a wavelength of 1550 nm.<sup>[68]</sup> Hexagonally arranged silicon nanoposts with different diameters were fabricated using electron-beam lithography and a hard-mask-assisted etching process, forming a polarization-independent meta-lens, as shown in Figure 4c. Scattering from the aperiodic HCTAs can be minimized by gradually changing the size of the nanoposts, and the desired phase profile can be precisely obtained owing to the weak coupling between the nanoposts. Using this design, up to 82% of the focusing efficiency could be realized, as shown in Figure 4d. Capasso et al. fabricated high-aspect-ratio meta-lenses based on geometric phase modulation. The meta-lens comprised titanium dioxide nanopillars with rectangular cross-sections, as shown in Figure 4e,<sup>[78]</sup> and has 86% focusing efficiency at a wavelength of 450 nm

and a diffraction-limited focusing spot, as shown in Figure 4f. Khorasaninejad et al. proposed dielectric meta-lenses consisting of nanopillars with circular cross-sections based on propagation phase modulation, as shown in Figure 4g.<sup>[69]</sup> The phase profile can be modified by changing the pillar diameter. This meta-lens can focus light down to an  $\approx 0.64 \lambda$  spot with 90% efficiency at a wavelength of 660 nm, as shown in Figure 4h. An aspheric meta-lens based on a Huygens metasurface platform was also introduced to provide up to 75% focusing efficiency, with a building block thickness of approximately 1/8 free-space wavelength.<sup>[56]</sup> Capasso et al.<sup>[82]</sup> proposed a solid-immersion transmissive meta-lens comprising GaSb posts fabricated directly on a GaSb substrate. These solid-immersion meta-lenses work for all incident polarizations and can achieve a maximum focusing efficiency of 80%.

For conventional lens, N.A. is defined as

$$\text{N.A.} = n \sin \theta \quad (10)$$

where  $n$  is the refractive index of the media in which the imaging lens lies and  $\theta$  is the maximum deflection angle at the meta-lens edge. In general, the N.A. of the meta-lens is related to i) the background refractive index, ii) the engineering of the focusing phases, and iii) distribution of the diffracted energy.<sup>[63,68,78,83–86]</sup>

The background refractive index can be adjusted by immersing the imaging system into a fluid such as oil for a higher  $n$  in Equation 10, which is applicable for both conventional lenses and meta-lenses. For example, Chen et al. demonstrated a planar meta-lens immersed in oil with an N.A. of 1.1 at a wavelength of 532 nm,<sup>[83]</sup> and Liang et al.<sup>[84]</sup> showed a crystalline silicon-based meta-lens with an N.A. of 1.48 in oil. The focusing phases can be engineered by controlling the lens morphology. Conventional lenses are based on phase accumulation through various optical paths from different radial positions modulated by the macroscopic lens thickness. To have a large N.A., a lens with a specific diameter should have a rapid phase

change at the edge. Namely, the edge should have an extremely large slope of thickness variation, which is a very challenging issue. In contrast, meta-lenses can overcome this limitation.<sup>[85]</sup> The rapid phase change can be realized by the compact arrangement of building blocks to generate arbitrary phases.<sup>[68,78]</sup>

The redistribution of the diffracted energy controls the defraction of light deflected by the building blocks, and hence concentrates the energy at specific positions. This is an advanced modulating mechanism that cannot be implemented using conventional lenses. For example, Kuznetsov et al.<sup>[63]</sup> demonstrated a meta-lens based on diffraction energy redistribution with a near-unity N.A., as depicted in Figure 5a. They employed asymmetric scattering from nanoantennas, where the number of diffraction orders and corresponding angles were determined by adjusting the periods of the unit cell, as shown in Figure 5b,c.

## 3.2. Aberration Correction

In an imaging scenario, the light emitted from a certain point of the object may not be focused at one unique pixel, which results in aberrations, including monochromatic or chromatic aberrations. Monochromatic aberration is caused by non-paraxial effects from monochromatic incident light, whereas chromatic aberration is caused by the structural dispersion of polychromatic incident light. Both effects lead to severe degradation of image quality. Therefore, aberration correction has become a key issue for high-quality imaging.

### 3.2.1. Monochromatic Aberration Correction

An ideal lens should perform high-resolution imaging with a sufficiently large field of view. However, the conventional lens is limited by monochromatic aberrations, including spherical aberration, coma aberration, astigmatism, and field curvature.

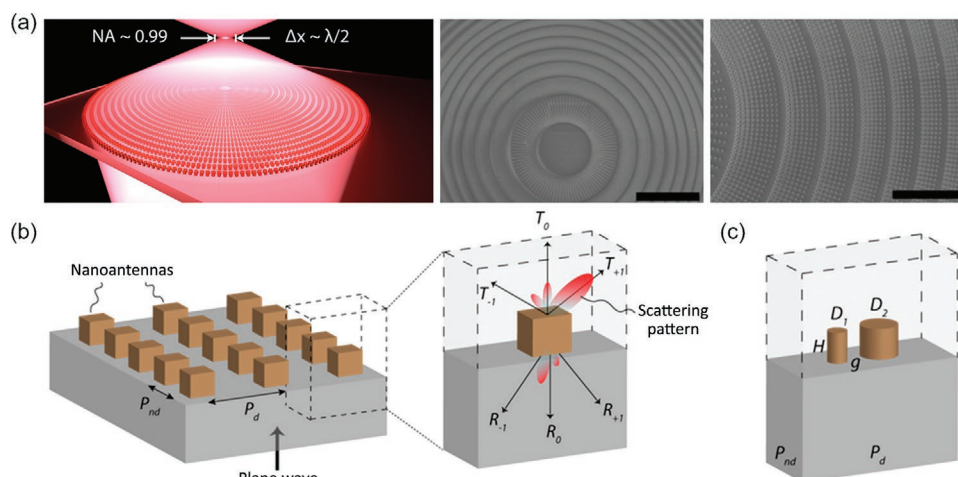


**Figure 5.** High numerical aperture imaging: a) Fabricated sample and SEM images of fabricated sample: low-magnification central and small-angle bending parts; b) nanoantenna arrays with controlled energy distribution among supported diffraction orders; c) asymmetric dimers array producing energy concentration to T+1 diffraction order, bending light at 82° for planar normally incident waves from substrate side at 715 nm. Reproduced with permission.<sup>[63]</sup> Copyright 2018, American Chemical Society.

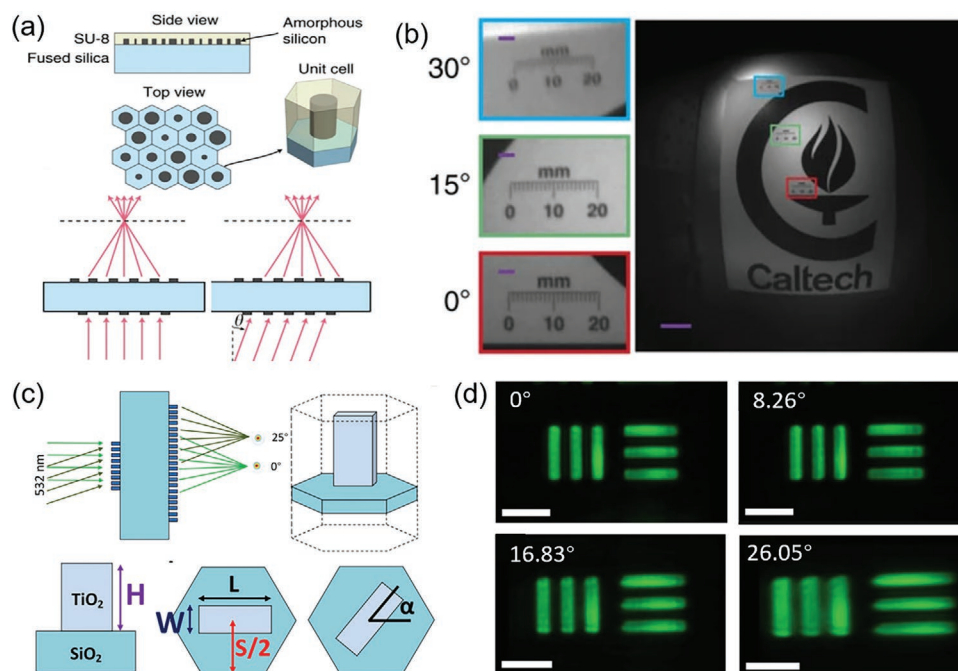


**Figure 6.** Monochromatic aberration correction: a) meta-lens doublet (top) one-sided metasurface configuration: amorphous silicon nanopillar array immersed in SU-8 polymer, (bottom) optical path for on and off-axis incidence; b) images using meta-lens doublet at different view angles (scale bar = 100  $\mu\text{m}$ ). Reproduced with permission.<sup>[87]</sup> Copyright 2016, The Authors, published by Springer Nature. c) Meta-lens doublet comprising of  $\text{TiO}_2$  nanopillars at different incident angles; d) images using meta-lens doublet with different incident angles (scale bars = 11  $\mu\text{m}$ ). Reproduced with permission.<sup>[89]</sup> Copyright 2017, American Chemical Society.

Spherical aberration occurs when rays from an on-axis point passing through the central and marginal regions of a lens are focused on different image planes. Coma aberration occurs when rays from an off-axis point are focused at different foci in the ideal image plane, forming a comet-like pattern. Coma aberrations are usually increased by enlarging the field of view. Astigmatism occurs when the convergent point of the meridian beam and the sagittal beam from an off-axis object point cannot be focused at the same position along the propagating direction, and the field curvature is the bending of the image plane. High-quality imaging requires a comprehensive solution to all these monochromatic aberrations.

For conventional lenses, the correction of monochromatic aberrations is realized by cascading multiple lenses, and this strategy is also valid for meta-lenses with additional benefits from miniaturizing the optical elements. Two metasurfaces can be integrated onto opposite sides of a single substrate, forming a doublet meta-lens. Faraon et al.<sup>[87]</sup> constructed a doublet meta-lens comprising of silicon nanopillars immersed in an SU-8 polymer (Figure 6a), and the phase profiles for the metasurfaces were optimized using ray tracing. Figure 6b confirms that the doublet meta-lens provided proper monochromatic aberration correction over a wide range of incident angles below 30° for the NIR band. Figure 6c shows a meta-lens doublet based on the Chevalier Landscape lens principle<sup>[88]</sup> in the visible region, incorporating aperture and focusing meta-lenses patterned on opposite silica substrate surfaces. This provides an aberration-free lens at a wavelength of 532 nm with N.A. = 0.44, and a 50° field of view. Figure 6d shows the angle-resolved images acquired by this meta-lens doublet.<sup>[89]</sup>

### 3.2.2. Chromatic Aberration Correction

For full-color imaging, chromatic aberrations must be corrected, which arise from structural and material dispersion. Polychromatic rays tend to focus at different spatial positions, which significantly degrade the image quality. Chromatic aberration correction for meta-lenses has been extensively studied. The operational wavelengths of the meta-lens have gradually been extended from single to multiple wavelengths and further to broadband ranges. Achromatic meta-lenses can be categorized into polarization-dependent and polarization-independent meta-lenses, depending on the incident light. The former is usually realized by tuning the geometry phase using anisotropic subwavelength building blocks, which offer higher design freedom, and the latter is realized by tuning the propagating phase using isotropic subwavelength building blocks.

*Achromatic Meta-Lens of Discrete Wavelengths:* The first reported achromatic meta-lens that operates at discrete wavelengths was a metasurface that comprised low-loss coupled rectangular dielectric resonators (Figure 7a). The correction follows the mechanism for dispersive phase compensation, that is, light can be focused at the same position for different specific operational wavelengths by artificially tuning the phase distribution on the metasurface and further compensating the phase difference caused by the dispersion. Figure 7b shows that the proposed achromatic meta-lens can focus 1300, 1550, and 1800 nm light with the same focal distance.<sup>[90]</sup> Another mechanism to correct polarization-dependent multiwavelength chromatic aberrations is analogous to holography. One can encode phase information for different wavelengths into a single

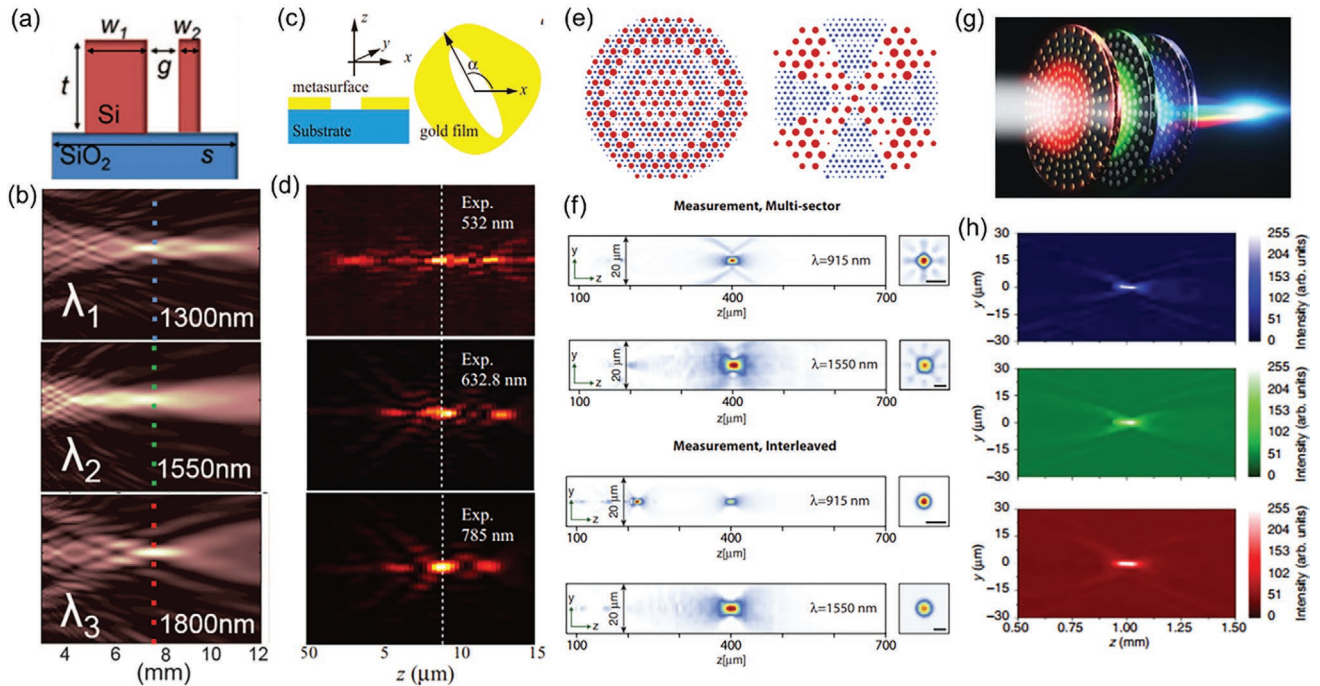


**Figure 7.** Multiwavelength achromatic meta-lenses. Low-loss coupled rectangular dielectric resonator based meta-lens: a) building blocks and b) intensity profiles for different incident wavelengths. Reproduced with permission.<sup>[90]</sup> Copyright 2015, American Association for the Advancement of Science. Nanoaperture based meta-lens: c) building blocks and d) intensity profiles for different incident wavelengths. Reproduced with permission.<sup>[91]</sup> Copyright 2015, Springer Nature. e) Two spatial multiplexing methods: (left) meta-atom interleaving and (right) large-scale segmentation. Reproduced with permission.<sup>[93]</sup> Copyright 2016, The Authors, published by Springer Nature. f) Intensity profiles for spatial multiplexing achromatic meta-lenses for different wavelengths in (left) yz and (right) focal planes;<sup>[93]</sup> g) vertical stack of three different meta-lenses and h) meta-lens intensity profiles for red, green, and blue light in the yz-plane. Reproduced with permission.<sup>[94]</sup> Copyright 2017, The Authors, published by Springer Nature.

metasurface using a plasmonic metasurface with spatially varying elliptic nano-apertures. Based on the spin-orbit interaction and geometric phase (Figure 7c,d), Zhao et al. showed focal intensity profiles at wavelengths of 532, 632.8, and 785 nm.<sup>[91]</sup> Both meta-lenses are polarization-dependent owing to their anisotropic building blocks.

Spatial multiplexing is also a practical approach to correct multiwavelength chromatic aberrations. Various metasurfaces with different operational wavelengths are combined in one surface area to provide the same focal length for multiple incident wavelengths. For example, Faraon et al.<sup>[92]</sup> fabricated high-contrast dielectric metasurfaces comprising of amorphous silicon nanoposts and proposed two different multiplexing methods: large-scale segmentation<sup>[93]</sup> and meta-atom interleaving (Figure 7e). The former divides the metasurface aperture into several large-scale segments, where each segment provides the same focal position for its specific operational wavelength. The latter means to mutually interleave different groups of meta-atoms within the same area, where each group provides the same focal position with its specific operational wavelength. According to their experimental results shown in Figure 7f, the focal point generated from the meta-atom interleaving meta-lens is of a better-defined circular shape. The operational wavelengths are 915 and 1550 nm with an N.A. of 0.46. Analogous to the cascading strategy for conventional lenses, meta-lenses with different operational wavelengths can be vertically stacked to form a multi-layer achromatic meta-lens

assembly. Each meta-lens operates independently of the incident wavelength with minimal spectral crosstalk between the lenses, achieving the same focal position. For example, Figure 7g shows a plasmonic achromatic meta-lens assembly,<sup>[94]</sup> comprising of disc-shaped nanoparticles of different sizes and materials, converging red, green, and blue light to the same focal point (Figure 7h). Although the concept is straightforward, the challenge here is the low transmission efficiency and high-precision alignment requirement.

*Achromatic Meta-Lens of Continuous Wavelength:* Multiwavelength corrections may not satisfy the increasingly stringent requirements of various applications owing to the discrete operating wavelengths. The achromatic meta-lenses with continuous operational wavelength are in high demand in imaging applications. Several narrowband achromatic meta-lenses have been reported,<sup>[95]</sup> realized by optimizing the structural parameters of the building block to simultaneously tune the phase and dispersion. The fabricated metasurface is comprised of titanium dioxide nanopillars with square cross-sections on a dielectric spacer layer atop a metallic mirror (Figure 8a). Nanopillars can provide phases from 0 to  $2\pi$  by changing their widths. Several widths that simultaneously provide the same phase but different dispersions at specific wavelengths are selected using an optimization algorithm. Figure 8b shows that the final meta-lens exhibits good achromaticity within 490–550 nm, with N.A. = 0.2 and 15% efficiency. Arbabi et al.<sup>[96]</sup> displayed a narrowband achromatic meta-lens comprising of amorphous silicon

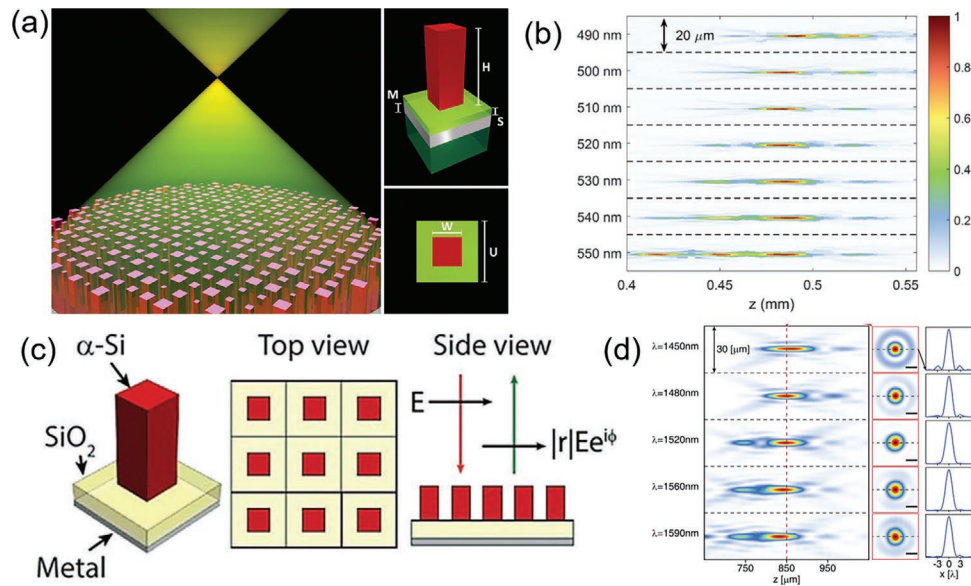


**Figure 8.** Narrowband achromatic meta-lenses: a)  $\text{TiO}_2$  nanopillars and b) intensity profiles for different incident wavelengths in the  $xz$ -plane. Reproduced with permission.<sup>[95]</sup> Copyright 2017, Optical Society of America. c) Amorphous silicon nanoposts and d) intensity profiles for different wavelengths in (left)  $xz$  and (right) focal planes (scale bars =  $2\lambda$ ). Reproduced with permission.<sup>[96]</sup> Copyright 2017, American Chemical Society.

nano-posts on a silicon dioxide spacer layer atop an aluminum reflector (Figure 8c). The working mechanism is similar to that of the previous meta-lens for working in the NIR region (1450–1590 nm) with N.A. = 0.28 and 50% efficiency (Figure 8d).

The achromatic bandwidth of the meta-lens must be further improved to realize feasible full-color imaging applications. In principle, this can be achieved by introducing appropriate phase compensation. In general, the meta-lens phase profile can be expressed as

$$\varphi(R, \lambda) = -2\pi \left( \sqrt{R^2 + f^2} - f \right) \frac{1}{\lambda} \quad (11)$$

where  $R$  is the radial coordinate,  $\lambda$  is the working wavelength in free space, and  $f$  is the designed focal length. We can express Equation (11) as a DP equation:<sup>[97]</sup>

$$\varphi_{\text{lens}}(R, \lambda) = \varphi(R, \lambda_{\text{max}}) + \Delta\varphi(R, \lambda) \quad (12)$$

for an achromatic meta-lens with operational wavelength  $\{\lambda_{\text{min}}, \lambda_{\text{max}}\}$ , where  $\varphi(R, \lambda_{\text{max}})$  is the focusing phase, which is only related to the nanostructure orientations, and  $\Delta\varphi(R, \lambda) = -2\pi \left( \sqrt{R^2 + f^2} - f \right) \left( \frac{1}{\lambda} - \frac{1}{\lambda_{\text{max}}} \right)$  is the phase dispersion. For a

chosen  $\lambda_{\text{max}}$ ,  $\Delta\varphi(R, \lambda)$  is linearly dependent on  $1/\lambda$  from the integrated-resonant phase, and the linearity guarantees continuous achromaticity.

Tsai et al.<sup>[97]</sup> developed a strategy to realize broadband achromaticity by merging an integrated-resonant phase response (wavelength-dependent) with the geometric phase (dispersion less). This strategy is experimentally realized by fabricating metallic IRUs, achieving broadband achromaticity within the visible (420–650 nm) and NIR (1200–1680 nm) regions<sup>[98]</sup> (Figure 9a–b, respectively). However, these meta-lenses operate in reflection mode.

Figure 9c shows a transmissive achromatic meta-lens with operational bandwidth almost covering the entire visible band (400–660 nm), using a principle similar to that of previous lenses. The meta-lens comprised solid and inverse GaN-based IRU elements.<sup>[99]</sup> The optimized sample achieved an average efficiency of 0.106 and 40% for achromatic full-color imaging.

This strategy is also feasible for the THz region. Li et al.<sup>[100]</sup> used solid and inverted C-shaped silicon nanostructures to implement an achromatic meta-lens operating within 0.3–0.8 THz with N.A. = 0.385 and 68% peak efficiency (Figure 9d).

An optimized strategy to correct chromatic aberrations is to simultaneously control the phase, group delay, and group delay dispersion. Given a bandwidth around  $\omega_d$ , the phase from Equation (11) can be expressed as a Taylor series expansion:

$$\varphi(R, \omega) = \varphi(R, \omega_d) + \left. \frac{\partial\varphi(R, \omega)}{\partial\omega} \right|_{\omega=\omega_d} (\omega - \omega_d) + \left. \frac{\partial^2\varphi(R, \omega)}{2\partial\omega^2} \right|_{\omega=\omega_d} (\omega - \omega_d)^2 + \dots \quad (13)$$

where  $\varphi$ ,  $\omega$ , and  $R$  are the phase, angular frequency, and radial coordinates, respectively, and the three terms represent phase, group delay, and group delay dispersion, respectively.

In the visible light range, group delay and group delay dispersion are of the order of femtoseconds (fs) and squared femtoseconds ( $\text{fs}^2$ ), which is generally neglected for conventional diffractive lenses but causes chromatic effects. However, all three terms can be artificially adjusted using a meta-lens when the following conditions are satisfied:

- i. Phase  $\varphi(R, \omega_d)$  is tuned to generate a spherical wavefront.
- ii. Group delay compensates for different wave packet arrival times at the focus.

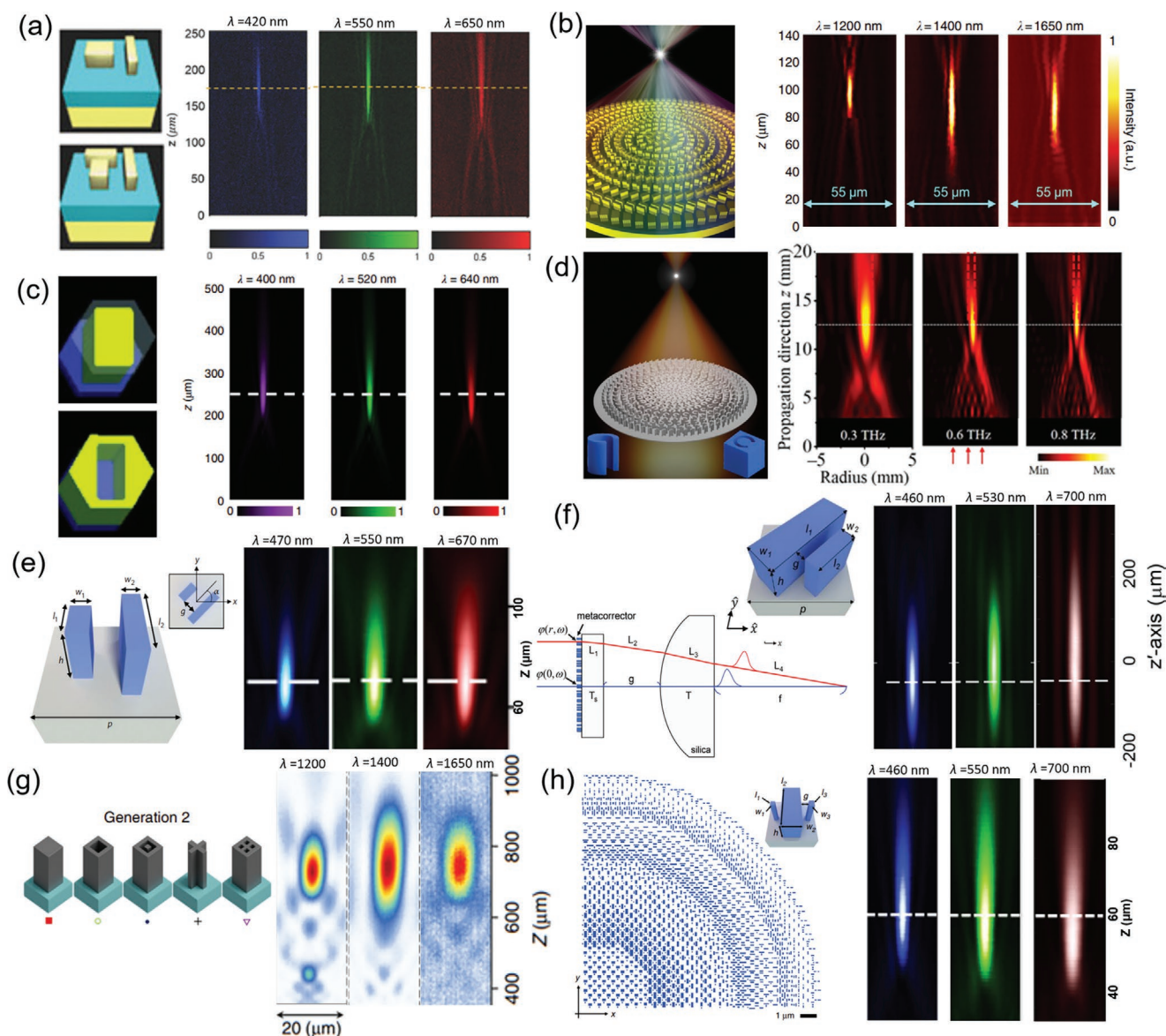


**Figure 9.** Broadband achromatic meta-lenses: building blocks and intensity profiles for different meta-lenses. a) Al IRUs, visible range (400–667 nm). Reproduced with permission.<sup>[97]</sup> Copyright 2018, Wiley-VCH. b) Au IRUs, NIR range (1200–680 nm). Reproduced with permission.<sup>[98]</sup> Copyright 2017, The Authors, published by Springer Nature. c) GaN IRUs, visible range (400–667 nm). Reproduced with permission.<sup>[99]</sup> Copyright 2018, Springer Nature. d) C-shaped unit elements, THz range (0.3–0.8 THz). Reproduced with permission.<sup>[100]</sup> Copyright 2019, Elsevier. e) Coupled TiO<sub>2</sub> nanostructures, visible range (470–670 nm). Reproduced with permission.<sup>[101]</sup> Copyright 2018, Springer Nature. f) Coupled TiO<sub>2</sub> nanostructures (hybrid lens), visible light range (460–700 nm). Reproduced with permission.<sup>[102]</sup> Copyright 2018, American Chemical Society. g) Amorphous silicon nanopillars, NIR (1200–1650 nm). Reproduced with permission.<sup>[103]</sup> Copyright 2018, The Authors, published by Springer Nature. h) Anisotropic TiO<sub>2</sub> nanostructures, visible light range (460–700 nm). Reproduced with permission.<sup>[104]</sup> Copyright 2019, The Authors, published by Springer Nature.

iii. Group delay dispersion guarantees identical outgoing wave packets.

Capasso et al.<sup>[101]</sup> demonstrated coupled phase-shift elements comprising of adjacent nanopillars in transmissive achromatic meta-lenses. The operating wavelength range is 470–670 nm with an efficiency of  $\approx 20\%$  at a wavelength of 500 nm (Figure 9e). The meta-lenses displayed diffraction-limited focusing and achromatic imaging across most of the visible range. However, the size of the lens is limited by the large

group delay, reaching only  $\approx 100 \mu\text{m}$ , which may not match the scale of common optical systems. To overcome this issue, they increased the lens size by combining metasurfaces with traditional refractive optical elements. Chromatic aberrations were corrected using the attached tunable phase and artificial dispersion metasurface, called the metacorrector (Figure 9f). The dimension of the final hybridized metasurface refractive optical device was 1.5 mm.<sup>[102]</sup>

The above broadband continuous achromatic corrections are polarization-dependent. For polarization-independent

**Table 1.** Performance of reported achromatic meta-lenses.

Material	Wavelength	Bandwidth <sup>a)</sup>	Diameter	N.A.	Eff.	Pol. <sup>b)</sup>	Ref.
TiO <sub>2</sub>	490–550 nm	60 nm/11.5%	200 μm	0.2	15%	CP	[95]
Si	1450–1590 nm	140 nm/9.2%	500 μm	0.28	50%	CP	[96]
Al	420–650 nm	230 nm/50%	41.86 μm	0.124	20%	CP	[97]
Au	1200–1680 nm	480 nm/33.3%	55.55 μm	0.217	8.4% <sup>c</sup>	CP	[98]
Au	1200–1680 nm	480 nm/33.3%	55.55 μm	0.268	12.44% <sup>c</sup>	CP	[98]
Au	1200–1680 nm	480 nm/33.3%	55.55 μm	0.324	8.56% <sup>c</sup>	CP	[98]
GaN	400–660 nm	240 nm/ 49%	25 μm	0.106	40%	CP	[99]
GaN	400–660 nm	240 nm/ 49%	25 μm	0.125	30%	CP	[99]
GaN	400–660 nm	240 nm/ 49%	25 μm	0.15	25%	CP	[99]
Si	375–1000 μm	0.5 THz/ 91%	10 mm	0.385	68% <sup>c</sup>	CP	[100]
TiO <sub>2</sub>	470–670 nm	200 nm/35%	25 μm	0.2	20%	CP	[101]
TiO <sub>2</sub>	470–700 nm	230 nm/ 40%	1.5 mm	0.075	35%	CP	[102]
Si	1200–1650 nm	450 nm/32%	200 μm	0.13	32%	NP	[103]
TiO <sub>2</sub>	460–700 nm	240 nm/40%	26.4 μm	0.2	35%	NP	[104]

<sup>a)</sup>The ratios between the bandwidth and the central wavelength of all the involved works are shown behind the symbol “/”; <sup>b)</sup>CP; circular polarization, NP; non-polarization.

applications, Shrestha et al.<sup>[103]</sup> proposed a polarization-insensitive achromatic meta-lens by modulating the propagation phase. The proposed amorphous silicon nanostructure had four-fold symmetry rather than just rotational symmetry to provide more geometric degrees of freedom without sacrificing polarization independence. They subsequently fabricated achromatic polarization-insensitive meta-lenses with up to 50% focusing efficiency in transmission mode across a continuous and broad bandwidth from 1200 to 1650 nm (Figure 9g). Capasso et al.<sup>[104]</sup> also reported a polarization-insensitive meta-lens for wavelengths ranging from 460 to 700 nm by using anisotropic nanofins to control phase, group delay, and group delay dispersion. Their results show a focusing efficiency of 35% (Figure 9h).

The results of various broadband achromatic meta-lenses are listed in **Table 1**, including their component materials, operational wavelengths, bandwidths, diameters (D), N.A., efficiencies (Eff.), polarization of the incident light (Pol.), and the corresponding references (Ref.).

### 3.3. Tunability

Tunability is another essential criterion for evaluating a meta-lens. High tunability facilitates the application of meta-lenses in novel optical systems. For example, dynamically tuning the focal length is of great significance in zooming devices, such as cameras, microscopes, telescopes, and endoscopes.<sup>[105,106]</sup> In conventional optical systems, zooming is realized by combining several lenses and changing their mutual axial distances, which enlarges the system scale and requires sophisticated integration techniques. Meta-lenses can overcome this limitation. The variation of the focal length can be realized by using a single dynamically tunable meta-lens, which is small and easy to integrate.

According to the operating mechanism, tunable meta-lenses are classified into two categories: inherent and external.

Inherent tuning is generated i) from the reconfigurable changes in the inherent structures of a meta-lens or ii) by reversibly varying the refractive indices of the inherent materials of a meta-lens. External tuning is generated from i) selective responses of a meta-lens to different external incident polarizations or ii) different responses of a set of meta-lenses where the spatial arrangement of every single meta-lens can be dynamically changed. In other words, inherent tuning is based on varying the optical properties of each individual meta-lens, and external tuning is based on varying the external light fields incident on each individual meta-lens.

#### 3.3.1. Inherent Tunability

*Reconfigurable Subwavelength Structures:* Tunable device performance can be achieved by adjusting i) the position or ii) the morphology of the building blocks. For the former, each building block provides a constant phase. Changing the position means to rearrange the modulators to generate a variable phase distribution. Changing the morphology refers to tuning the generated phase of each modulator, which are fixed at a constant position. Both cases lead to an integral response of the meta-lens function.

Polydimethylsiloxane (PDMS) is one of the most widely used stretchable materials. It is used for generating reconfigurable meta-lenses. The position adjustment of the building blocks is achieved by external mechanical forces.<sup>[107]</sup> For example, Ee et al. proposed a mechanically tunable metasurface at a wavelength of 632.8 nm, which acts as an ultrathin flat zoom lens (**Figure 10a**).<sup>[108]</sup> The relative positions of the plasmonic Au nanorods can be continuously changed by stretching the substrate, thus tuning the wavefront shape. Figure 10b shows a flat meta-lens fabricated on PDMS for various focal lengths 150–250 μm with corresponding optical zoom around 1.7. Their work shows the realization of a tunable lens with nanoscat-terers embedded in an elastomeric substrate.<sup>[108]</sup>

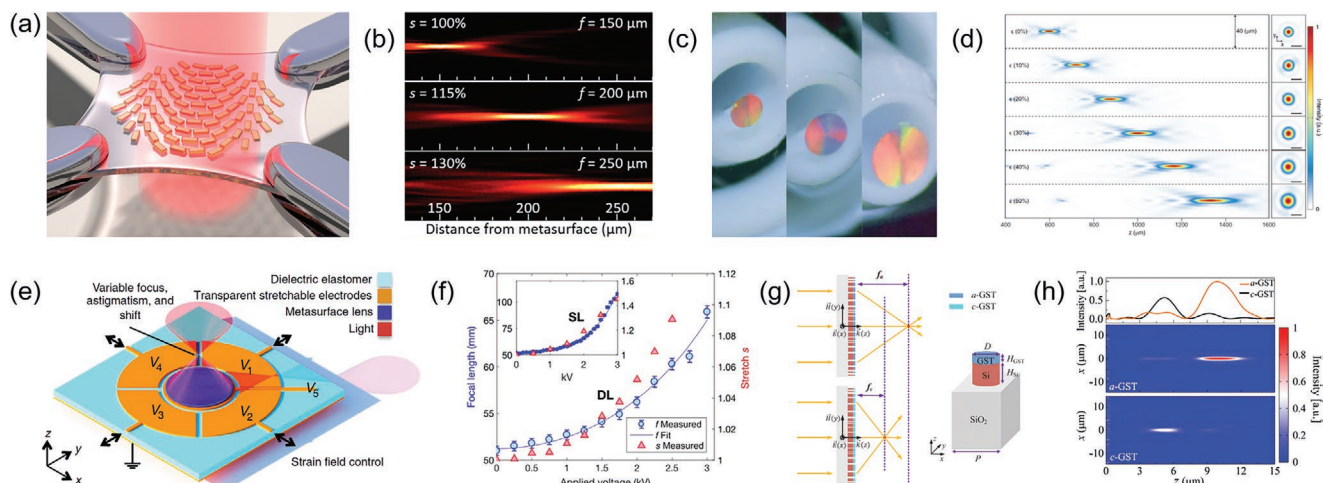


**Figure 10.** Inherent tunability: a) tunable metasurfaces on a stretchable polydimethylsiloxane (PDMS) substrate;<sup>[108]</sup> b) longitudinal beam profiles generated from the flat zoom lens transmission side with  $s = 100\%$  (top),  $115\%$  (middle), and  $130\%$  (bottom). Reproduced with permission.<sup>[108]</sup> Copyright 2016, American Chemical Society. c) Highly tunable elastic dielectric metasurface lenses;<sup>[109]</sup> d) measured optical intensity profiles for radially strained metasurface microlenses ( $\epsilon = 0\text{--}50\%$ ) in the axial plane (left) and the focal plane (right) (scale bars =  $5\ \mu\text{m}$ ). Reproduced with permission.<sup>[109]</sup> Copyright 2016, Wiley-VCH. e) Meta-lens and dielectric elastomer actuator (DEA) with five addressable electrodes to electrically control metasurface strain field.<sup>[112]</sup> f) Measured focal length tuning using center electrode  $V_5$  for double-layer and single-layer (inset) devices, blue circles = device focal length measured optically with respect to applied voltage. Reproduced under the terms of the Creative Commons Attribution Non-Commercial License 4.0 (CC BY-NC).<sup>[112]</sup> Copyright 2018, The Authors, some rights reserved; exclusive license American Association for the Advancement of Science. g) Bifocal meta-lens converging light to two different focal distances for amorphous germanium antimony telluride (*a*-GST) or crystalline germanium antimony telluride (*c*-GST) and a single unit cell;<sup>[120]</sup> h) simulated *a*-GST and *c*-GST intensity profiles in the  $x\text{--}z$  plane. Reproduced with permission.<sup>[120]</sup> Copyright 2019, IOP Publishing.

Kamali et al.<sup>[109]</sup> demonstrated a highly tunable dielectric meta-lens comprising of subwavelength thick silicon nanoposts encapsulated in PDMS (Figure 10c). The weak optical coupling between the nanoposts allows the tunable meta-lens to operate at a wavelength of  $915\ \text{nm}$  through radial strain, providing an efficiency of  $\approx 50\%$ , focal distance tunability from  $600\ \mu\text{m}$  to  $1400\ \mu\text{m}$ , and polarization independence (Figure 10d). Vamvakas et al.<sup>[110]</sup> adopted a similar approach to realize the first reflective mechanical tunable meta-lens at a wavelength of  $670\ \text{nm}$  based on gap surface plasmonic resonators. The focal length could be continuously adjusted by up to  $45\%$  with  $20\%$  lateral PDMS stretching, while maintaining a high focusing performance comparable to that reported in ref. [109]. Although meta-lenses based on flexible substrates can support focal length tuning, most reported works<sup>[108–110]</sup> required an external stretching mechanism that had a long response time.

Tunable meta-lens systems can be realized by combining metasurface optics and dielectric elastomer actuators (DEAs), sometimes referred to as artificial muscles.<sup>[111,112]</sup> DEA is a type of electroactive polymer that forms a compliant stretchable parallel plate capacitor that can be controlled by applying an external electric field or voltage.<sup>[111,113]</sup> She et al. recently demonstrated an electrically tunable meta-lens,<sup>[112]</sup> based on bonding a metasurface with DEA to couple the meta-lens profile to the voltage-induced stretching, as shown in Figure 10e. Large-area tunable meta-lens systems controlled by artificial muscles can simultaneously provide focal length tuning ( $>100\%$ ) (Figure 10f), on-the-fly astigmatism, and image shift corrections.<sup>[112]</sup> DEA-based tunable meta-lens systems are promising for future optical microscopes requiring a fully automatic operation and metasurface-based optical systems that require

astigmatism and image shift tuning. However, these systems require high voltage (kV range) because the tuning mechanism depends on the capacitive electrostatic force to compress the elastomer.<sup>[114,115]</sup>

Changing the morphology of the building blocks is another feasible method. Zhu et al.<sup>[116]</sup> reported a proof-of-concept for a planar random access reconfigurable metamaterial (RARM), where resonant properties for individual split rings can be continuously controlled by changing the metal filling fraction. The RARM-based meta-lenses achieve tunable focal distance by adjusting the spatial phase gradient.

**Reversible Materials:** Another strategy to inherently tune the meta-lens performance is by using reversible materials, whose refractive indices can dynamically respond to heat or electric stimulations. Consequently, the phase modulation of each sub-wavelength structure is changed, resulting in an integrated variation of the meta-lens functions.

The phase-change material is a heat-responsive material in which the transition of crystalline states, and hence the refractive index is influenced by temperature. It can be used to compose reversibly tunable meta-lenses.<sup>[117,117–120]</sup> For example, Li et al.<sup>[120]</sup> proposed an all-dielectric metasurface comprising of germanium-antimony-telluride/silicon hybrid nanopillars to achieve a bifocal meta-lens in the NIR, as shown in Figure 10g. The two different focal lengths are shown in Figure 10h.

Graphene, which is a monolayer of hexagonally arranged carbon atoms, is an electrically responsive material. Its optical properties can be tuned by the applied voltage, which influences the Fermi energy. It has been theoretically predicted to be a suitable material for making reversibly tunable meta-lenses.<sup>[121–126]</sup> However, the experimental fabrication of

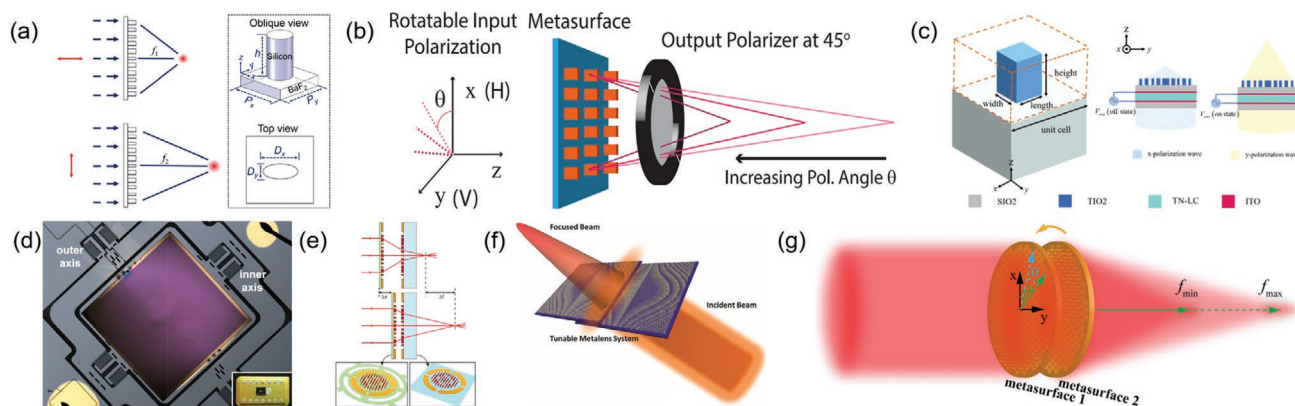


**Figure 11.** External tunability: a) polarization-multiplexing meta-lens principle: meta-lens focuses vertical or horizontal polarized light onto independent focal planes. Perspective and top view of the meta-lens unit cell formed by an elliptical amorphous silicon nanopillar sitting on a BaF<sub>2</sub> substrate. Reproduced with permission.<sup>[77]</sup> Copyright 2018, Optical Society of America. b) Principle of operation: linearly polarized light passes through a meta-lens and an output polarizer oriented at 45°. The focal length changes as the input polarizer is rotated. Reproduced with permission.<sup>[133]</sup> Copyright 2019, American Chemical Society. c) Unit cell structure for electrically modulated meta-lens combined with TN LCs. Reproduced with permission.<sup>[135]</sup> Copyright 2020, Optical Society of America. d) Micro-electro-mechanical system (MEMS) scanner with top flat lens (optical microscope image) indicating the rotational axes, inset: device mounted on dual in-line package ready for electrostatic actuation. Reproduced under the terms of the Creative Commons Attribution (CC BY) License.<sup>[137]</sup> Copyright 2018, The Authors. e) Proposed tunable lens comprising of stationary lens on a substrate and moving lens on a membrane. Reproduced with permission.<sup>[138]</sup> Copyright 2018, Springer Nature. f) Proposed tunable meta-lens system comprising of two cubic metasurface phase plates actuated laterally. Reproduced with permission.<sup>[146]</sup> Copyright 2018, Optical Society of America. g) Varifocal meta-lens comprising of combined metasurfaces with mutual rotation. Reproduced with permission.<sup>[153]</sup> Copyright 2019, AIP Publishing.

graphene-based tunable meta-lenses is still challenging and limited by the fabrication techniques.

Varifocal meta-lenses have been reported based on electro-thermo-optical systems.<sup>[127,128]</sup> Electrically controlled resistive spirals induce thermal refractive index variation in a thermo-responsive material, such as PDMS. The thermo-optical effect is precisely used to control the optical system.

### 3.3.2. External Tunability

**Incident Polarizations:** External tunability involves controlling the responses of a meta-lens or a meta-lens assembly to external stimuli without changing the functions of any meta-lens. The most straightforward stimulation is variable incident polarizations. Some anisotropic meta-lenses provide different responses to reversible polarization changes and can be used as tunable devices.

The most basic tunability is the alternative switching between two responsive states.<sup>[78,129–132]</sup> For example, Zheng et al. proposed a dual field-of-view step-zoom meta-lens to realize reconfigurable optical zooming through the control of the polarization states without changing the focal plane.<sup>[129]</sup> Fan et al. showed a single-layer, all-dielectric, polarization-multiplexing meta-lens based on an anisotropic dielectric waveguide phase shifter.<sup>[78]</sup> The meta-lens switched the focal length between two focal planes by simply changing the linear polarizations of the incident light (Figure 11a). For the continuous variation of the focal length, Aiello et al.<sup>[133]</sup> demonstrated a varifocal meta-lens based on the rotational polarization of linearly polarized incident light, as shown in Figure 11b. The focal length can be tuned from 220 to 550 μm. Furthermore, polarization-responsive meta-lenses can be integrated with polarizers to realize the combined function of incident

polarization modulation and focusing tunability within a single miniaturized device. For example, a polarizer comprising twisted-nematic liquid crystals can be cascaded with anisotropic meta-lenses, as shown in Figure 11c.<sup>[134,135]</sup>

**Spatial Arrangement:** The spatial arrangement of the specific focusing responses can be realized by adjusting the positions of the beam-to-lens or lens-to-lens. For a single meta-lens, the position or orientation angle of the lens can be changed to change the focal point. For an assembly of multiple meta-lenses, the positions of each meta-lens in the assembly will be changed to tune the internal light fields.

The micro-electro-mechanical system (MEMS) is an efficient platform for manipulating meta-lenses and provides the distinct advantage of precise and rapid movements.<sup>[136]</sup> Roy et al. demonstrated a monolithic MEMS-integrated meta-lens for focusing mid-IR light.<sup>[137]</sup> The orientation angle of the meta-lens could be electrically controlled along two orthogonal axes by ±9°, maintaining ≈83% focusing efficiency, as shown in Figure 11d. Faraon et al.<sup>[138]</sup> also presented an MEMS-integrated meta-lens system. They fabricated a proof-of-concept meta-lens doublet comprising of converging and diverging meta-lenses at a wavelength of 915 nm (Figure 11e). They experimentally demonstrated tunable lenses with over 180 diopters change in optical power by actuating the axial interval between two meta-lenses and generating over 60 μm focal length variation (i.e., from 565 to 629 μm). MEMS-integrated meta-lens systems are promising for real-time applications such as fast-scanning endoscopes, projection imaging, and LIDAR scanners.<sup>[139,140]</sup>

For conventional lens systems, the Alvarez principle is widely used to generate variable focal lengths.<sup>[141–148]</sup> An Alvarez system incorporates two opposite parallel lenses, where the depth of focus is increased, and the phase profile is defined by a cubic function, leading to focal length variation caused by

lateral displacement.<sup>[142–145]</sup> This method is also applicable to meta-lenses. Zhan et al.<sup>[144]</sup> showed a proof-of-concept Alvarez meta-lens comprising of silicon nitride nanoposts. It is a large-area device with a varifocal length of 2.5 mm. The aperture of this system was subsequently expanded up to 1 cm to realize a larger varifocal length reaching 6.62 cm, as shown in Figure 11f.<sup>[146]</sup> Alvarez lenses are promising for large-aperture and large-focal-length applications, such as eyeglasses, mixed reality displays, microscopy, and planar cameras.<sup>[147,148]</sup> A derivative of the Alvarez system is also presented where the two lenses are coaxially rotated rather than being parallelly moved, which is inspired by the Moiré lens.<sup>[149–153]</sup> Cui et al.<sup>[151]</sup> proposed a rotationally tunable polarization-dependent varifocal metasurface, and Yilmaz et al.<sup>[152]</sup> demonstrated a polarization-independent varifocal metasurface. Subsequently, Guo et al.<sup>[153]</sup> fabricated a 3.5× continuous varifocal meta-lens in the microwave band, with an improved N.A. ranging from 0.56 to 0.92 (Figure 11g). Both the translational and rotational versions of the Alvarez systems could be manipulated in a straightforward manner and provide good tunability of the optical responses. However, both the systems require high-precision alignment and manipulation techniques when the dimensions of the meta-lenses are down to a microscopic scale. Misalignment decreases the focusing efficiency and imaging quality.

## 4. Applications

### 4.1. Polarization Imaging System

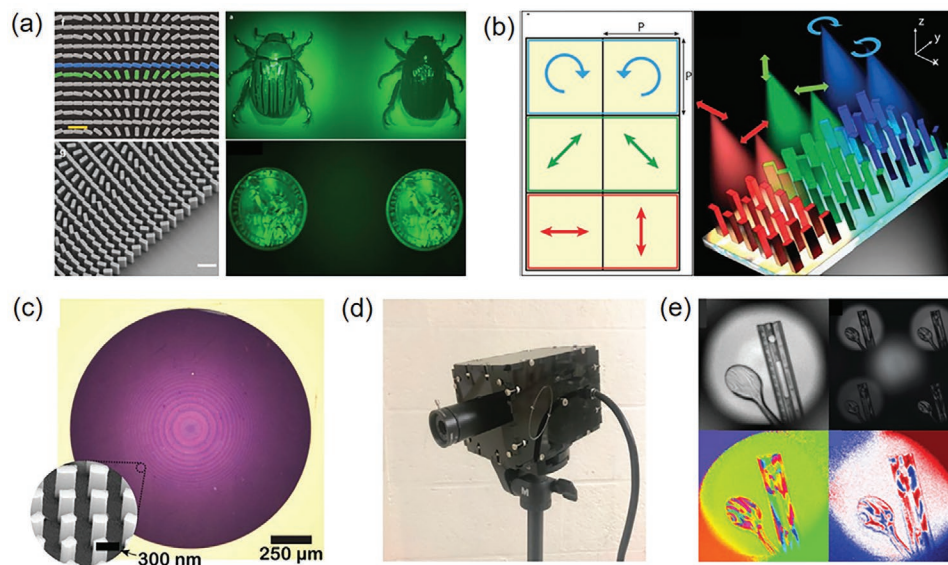
The conventional polarization imaging system typically includes the optical components of prisms and waveplates. These

systems usually have complex setups and also suffer from low polarization contrast ratio. The polarization-dependent nano-antennas of the meta-lens provide a tremendous intrinsic advantage for polarization imaging applications. meta-lenses offer high polarization contrast ratio for polarization imaging applications.<sup>[6,8,154]</sup>

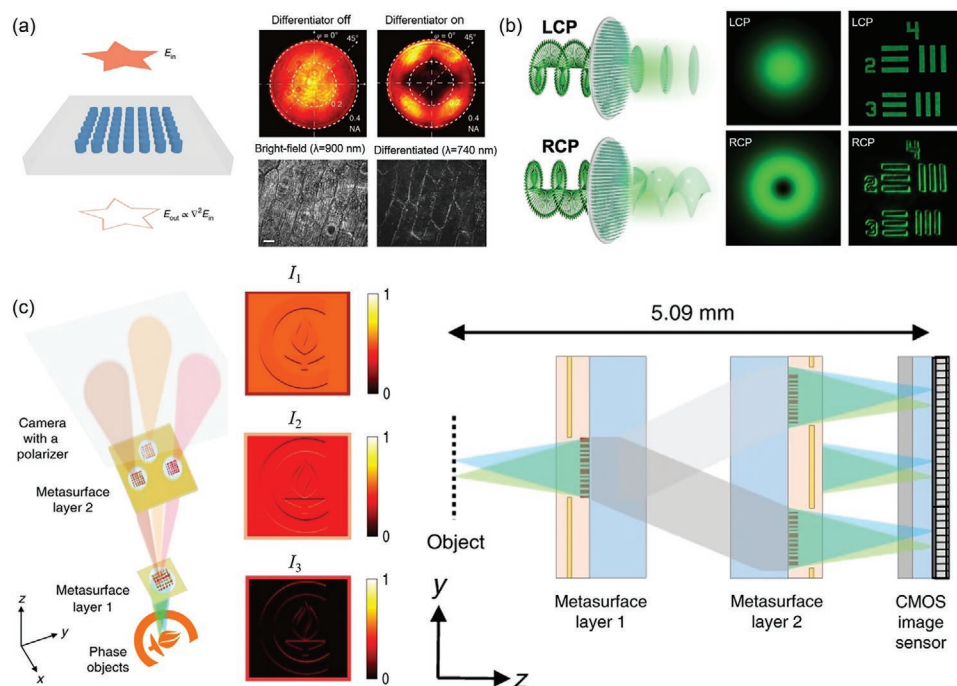
Figure 12a shows a dielectric meta-lens based on a geometrical phase design that can simultaneously capture two spectrally resolved images of a biological specimen within the same field of view.<sup>[80]</sup> Since the geometric phase is chiral sensitive, the biological specimen's circular dichroism can be probed across the whole visible spectrum using only a single meta-lens and camera, without additional optical components. Thus, metasurface polarization optics allows two arbitrary and independent phase profiles to be imposed on a pair of orthogonal polarization states.<sup>[58,155–157]</sup> This approach combines geometric and propagation phase modulation.

Figure 12b shows a compact metasurface device, comprising of three different meta-lenses to split and focus light into six different pixels on an image sensor for three different polarizations.<sup>[158]</sup> An image of a complicated polarization object could be captured with this device. Thus, the device serves as a full-Stokes polarization camera for the NIR region. A generalized Hartmann–Shack polarimetric beam profiler has been demonstrated using a similar method for a wavelength of 1550 nm, which allows the simultaneous measurement of the phase and spatial polarization profiles for an optical beam.<sup>[159]</sup> These silicon-based metasurface arrays can be mass-produced using a complementary metal-oxide-semiconductor (CMOS) compatible process.

Rubin et al.<sup>[160]</sup> proposed a matrix Fourier optics concept to design metasurface gratings for implementing arbitrary



**Figure 12.** Multispectral chiral meta-lens: a) (left) SEM images of top and side views and (right) captured images from color camera of (top) beetle and (bottom) one-dollar coin, where left and right images were formed by left circularly polarized and right circularly polarized reflected light, respectively. Reproduced with permission.<sup>[80]</sup> Copyright 2016, American Chemical Society. b) Metapixels for the polarization camera: (left) three pairs of independent polarization bases selected to measure Stokes parameters for each meta-pixel array, (right) 3D metapixel splitting and focusing of different polarization states to different positions. Reproduced with permission.<sup>[158]</sup> Copyright 2018, American Chemical Society. c) Metasurface-based grating optical microscope image, inset: SEM birefringent TiO<sub>2</sub> nanopillars; d) imaging system; e) plastic ruler and spoon captured with the polarization camera. Reproduced with permission.<sup>[160]</sup> Copyright 2019, American Association for the Advancement of Science.



**Figure 13.** 2D photonic crystal device: a) the device (left) acting as a Laplacian operator (right) for measured back focal plane (top) and onion epidermis cell sample images (bottom). Reproduced with permission.<sup>[164]</sup> Copyright 2020, Springer Nature; b) (left) spin multiplexed metasurface concept, (right) simulated and experimental conversion between bright-field and phase-contrast imaging modes. Reproduced with permission.<sup>[165]</sup> Copyright 2020, American Chemical Society. c) Quantitative phase microscope (left) miniaturized optical system, (center) three differential interference contrast images, (right) the two metasurface layers. Reproduced with permission.<sup>[166]</sup> Copyright 2019, Springer Nature.

polarization analysis. A compact full-Stokes polarization camera was constructed based on this metasurface grating with no additional optical components, providing excellent polarization photography, as shown in Figure 12c–e. Polarization imaging has also been demonstrated for mid-IR using an all-dielectric metasurface<sup>[161]</sup> and vertically stacked plasmonic metasurface.<sup>[162]</sup>

#### 4.2. Phase Imaging System

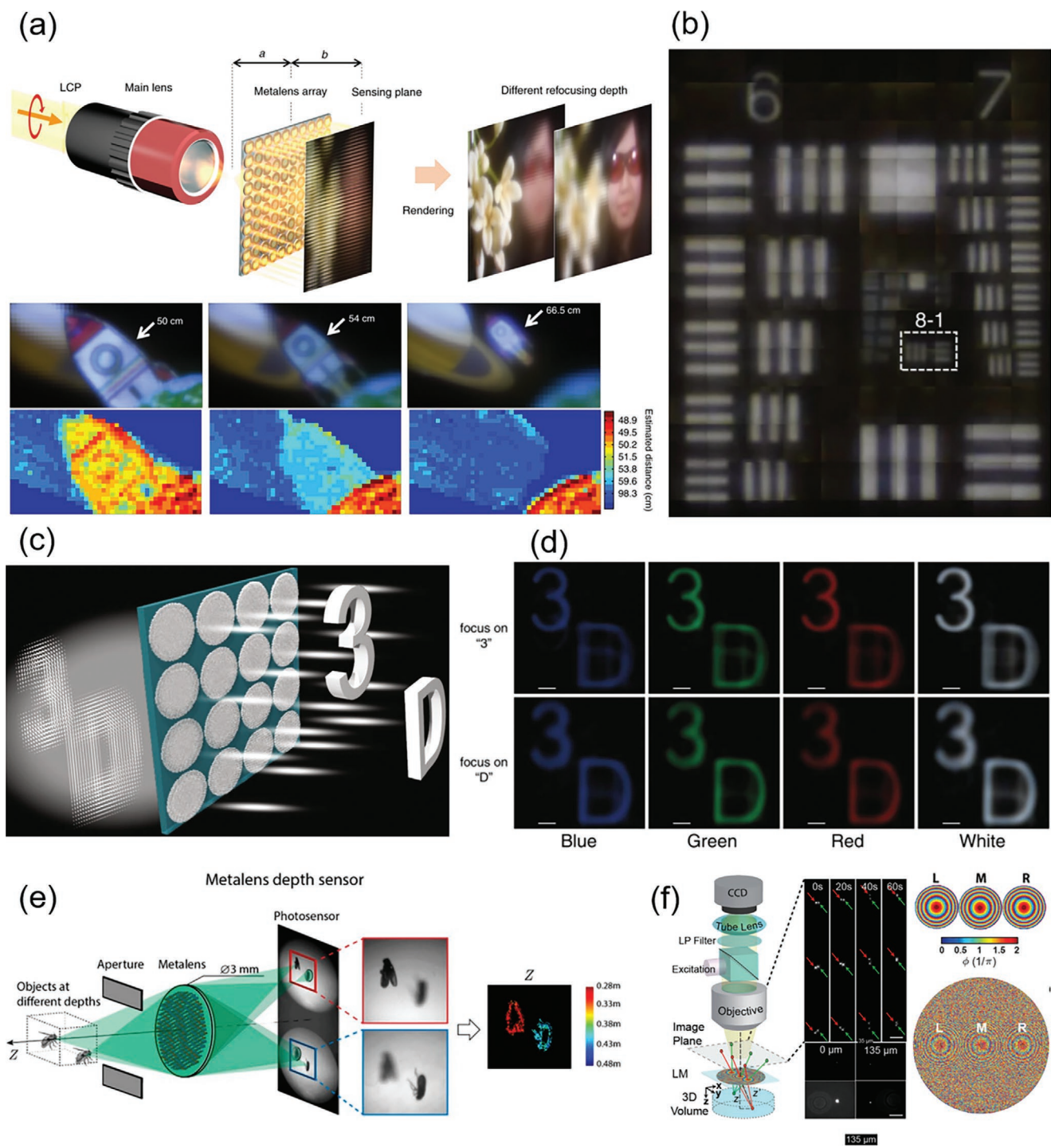
Phase imaging of transparent objects is an important optical imaging method in biological studies and medical diagnosis. The details of the bio-structures can be revealed by the phase contrast. Edge enhancement is a phase imaging technique that can be accomplished by using spatial differentiation or Fourier transform based on multiple lenses and filters. The results show that metasurfaces offer an excellent advantage for this application.<sup>[163–166]</sup> **Figure 13a** depicts a silicon-based metasurface for a direct differentiation image.<sup>[164]</sup> The metasurface differentiator is a Si nanopillar photonic crystal that can convert an object wave,  $E_{in}$ , into its second-order derivative, that is,  $E_{out} \propto \nabla^2 E_{in}$ , allowing direct edge detection. This new approach significantly reduces the size requirement of the optical system.

Figure 13b shows a recently proposed spin multiplexed metasurface-based imaging system to realize spiral phase-contrast imaging.<sup>[165]</sup> This system can switch between bright-field and phase-contrast imaging modes depending on the chirality of the incident light. Quantitative phase imaging can provide

accurate phase characterization. Conventionally, it requires a complicated and bulky optical interference system. Figure 13c displays a miniaturized quantitative phase microscope based on two dielectric metasurface layers and the classical differential interference contrast approach.<sup>[166]</sup> This microscope can simultaneously obtain three differential interference contrast images to form a quantitative phase gradient image based on the multifunctionality of this specific dielectric metasurface. The volume size of the optical imaging system is  $\approx 1\text{mm}^3$ , which is very useful for new applications in biomedical imaging and machine vision.

#### 4.3. Light-Field Camera

Light-field imaging acquires high-dimensional radiance information of the light field. Ideally, the image can provide the spatial coordinates of the position, velocity, and spectral information of the object. **Figure 14a** shows a full-color light-field imaging system that can capture multi-dimensional light-field information using a GaN achromatic meta-lens array.<sup>[167,168]</sup> The multiple images captured at the sensing plane provide the depth of the rendered image, as shown in Figure 14a. The depth of the object obtained by light-field imaging also provides the velocity of the object in the time frame. This full-color light-field optical system can image the 1951USAF resolution test target with a diffraction-limited resolution of  $\approx 1.95\ \mu\text{m}$  under incoherent normal white light illumination, as shown in Figure 14b.<sup>[167]</sup>



**Figure 14.** Meta-lens light-field applications: a) (top) light-field imaging and rendered images, (middle) rendered images focusing on the rocket with different depths, (bottom) corresponding estimated depth maps; b) rendered image formed by achromatic meta-lens array with incident white light. Reproduced with permission.<sup>[167]</sup> Copyright 2018, Springer Nature. c) Integral imaging with achromatic meta-lens array with incident white light; d) reconstructed images with different depth planes. Reproduced with permission.<sup>[169]</sup> Copyright 2019, The Authors, published by Springer Nature. e) Depth sensor estimation process. Reproduced with permission.<sup>[170]</sup> Copyright 2019, The Authors, published by National Academy of Sciences. f) Light-field metasurface imaging two beads at different  $(x,y,z)$  locations. Reproduced with permission.<sup>[171]</sup> Copyright 2019, American Chemical Society.

Fan et al.<sup>[169]</sup> reported integral imaging to capture and reconstruct light-field information. The workflow principle is opposite to that of the light-field camera. Figure 14c shows

that integral imaging encodes 3D scenes with computational algorithms and reconstructs optical images in free space. A polarization-insensitive silicon nitride achromatic meta-lens

array is used for the reconstruction in the visible region to render 3D scenes. This meta-lens array can realize diffraction-limited focusing and white light integral imaging, as shown in Figure 14d.

Guo et al.<sup>[170]</sup> proposed a depth perception method inspired by jumping spider eyes. They introduced a meta-lens depth sensor, where the meta-lens splits the light through an aperture and forms a pair of differently defocused images from the two halves of a single planar photosensor. An efficient algorithm is then employed to calculate the depth from these images, as shown in Figure 14e. This method captures two different images in a single shot rather than sequentially and requires relatively less computation.

Holsteen et al.<sup>[171]</sup> also proposed a light-field metasurface for high-resolution single-particle tracking. The surface interleaves three meta-lenses to achieve three different perspectives in a single image, and the depth information can be obtained by measuring the lateral separation between the two outermost bead images (Figure 14f). This approach can realize simultaneous three-dimensional imaging without substantially modifying the conventional microscope and only requires the addition of a patterned coverslip on top of the sample.

#### 4.4. Other Multi-Functional Applications

The applications of multi-functional meta-lens optical systems are booming.<sup>[172–179]</sup> For example, these optical systems are now used in endoscopic imaging for acquiring high-resolution optical images for clinical applications. Pahlevaninezhad et al.<sup>[175]</sup> integrated a silicon-based meta-lens into an endoscopic optical coherence tomography catheter. They achieved near-diffraction-limited imaging at an extended depth of field without complex component arrangements in the optical system, as shown in Figure 15a. They were able to capture magnified images of flesh fruit using an endoscope. The cells could be easily identified, and the cellular walls could be clearly seen.

Conventional tomography imaging is usually achieved by scanning with bulky mechanical components. Figure 15c shows a recently reported aplanatic meta-lens with strong chromatic dispersion employed to achieve high-resolution spectral tomographic imaging without additional mechanical components.<sup>[176]</sup> The aplanatic design results in imaging with high transverse and longitudinal resolution.

Two-photon microscopy is an essential fluorescence microscopy imaging technique that provides superior tissue imaging. Figure 15b shows a new two-photon fluorescence microscopy technique based on a double-wavelength meta-lens.<sup>[177]</sup> The meta-lens has the same focal length for excitation and emission frequencies. The images are comparable to those captured with conventional refractive objectives.

Chen et al.<sup>[79]</sup> experimentally demonstrated a multiplex color router with a GaN-based meta-lens to guide primary colors into desired spatial positions, as shown in Figure 15d. The proposed color router achieved 27.56%, 37.86%, 15.9%, and 38.33% efficiency for the R, G<sub>1</sub>, B, and G<sub>2</sub> color channels, respectively. This technology can be highly beneficial for practical CMOS image sensor applications. Lee et al.<sup>[178]</sup> proposed a new meta-lens display technology based on anisotropic nanostructures to

realize a compact near-eye display for augmented reality with a wide field of view, as shown in Figure 15e. They implemented a multi-functional meta-lens as a transparent medium for simultaneous light transmission from real-world scenes and as an eyepiece for the virtual world. Faraji-Dana et al.<sup>[179]</sup> proposed a miniaturized spectrometer made from a folded metasurface optical system. The system was found to have a resolution of around 1.2 nm for the wavelength range from 760 to 860 nm, as shown in Figure 15f.

Meta-lenses can also be applied in nonlinear optics. Schlickriede et al.<sup>[180]</sup> recently demonstrated an ultrathin nonlinear meta-lens implementation employing second-harmonic generation of gold nanoantennas. The phase profile for the proposed meta-lens can be obtained by the nonlinear geometry phase from the antenna orientation angle and the polarization state of the incident light. This approach provides a new platform for manipulating nonlinear optical waves.

Meta-lenses have also been used for optical quantum information technology related applications. A high-dimensional entanglement and multiphoton-state generation optical chip was introduced by Li et al.<sup>[181]</sup> They demonstrated a high-dimensional quantum entangled light source by using a 10 × 10 meta-lens array chip integrated with a thin beta barium borate, BaB<sub>2</sub>O<sub>4</sub>, crystal. This optical quantum chip could generate 100-path entangled photon pairs, and multi-dimensional tomography with high fidelity was achieved, as shown in Figure 15g. This work proposes stable, compact, controllable high-dimensional quantum chips capable of room temperature operation for optical quantum information applications.<sup>[181]</sup>

## 5. Prospects of Meta-Lens

Many people would like to make large-diameter meta-lenses to replace the traditional optical glass lenses. Some intentions even ask for the cheap and fast methods to produce the special meta-lens on a meter scale. The challenge is much more than the current state-of-the-art semiconductor electronic nanodevice production on 12-inch wafer. However, we consider the future prospects of meta-lens in terms of its high efficiency, novel functionality, better performance, compact size, customizability, low energy consumption, scalability, flatness, and CMOS mass production process compatibility. For example, the advantage of the small diameter of the meta-lens is that the small aperture provides a large depth of field. The intrinsic advantages of the artificial nanoantennas of the meta-lens include the characteristics of resonant wavelength, polarization, angular momentum, nonlinearity, spontaneous parametric up/down conversion, etc. Pioneering works in optical light-field, polarization, and phase imaging are just the beginning of the story. Computational methods can be used in metaoptics imaging systems for design, optimization, and signal processing. Recent results indicate that the unprecedented functions of the meta-lens can be further enhanced by using computational methods.<sup>[182]</sup>

Meta-lenses with novel functions can be incorporated into many existing optical systems to achieve new features and a more compact configuration. For example, meta-lenses can be used for optical diffusion, filtering, beam shaping and/or splitting, pattern generation, multi-dimensional light-field

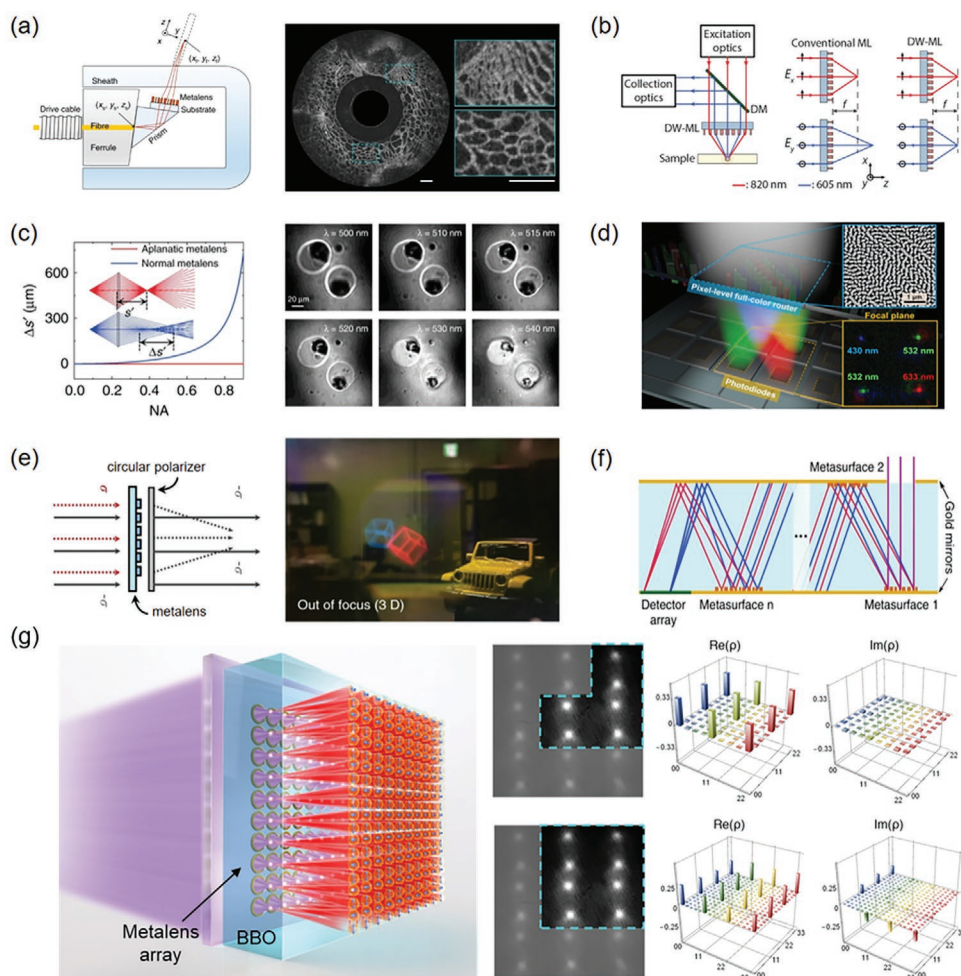


**Figure 15.** a) Nano-optic endoscope: (left) device details, (right) optical coherence tomography images for fruit flesh. Reproduced with permission.<sup>[175]</sup> Copyright 2018, Springer Nature. b) Two-photon microscopy with a double-wavelength meta-lens (DW-ML) objective lens. Reproduced with permission.<sup>[177]</sup> Copyright 2018, American Chemical Society. c) Aplanatic meta-lens for 3D tomographic imaging, (left) dependence of spherical aberration ( $\Delta s'$ ) on N.A., inset: corresponding ray tracing results for lens with N.A. = 0.78, (right) tomographic images at different wavelengths. Reproduced with permission.<sup>[176]</sup> Copyright 2019, Springer Nature. d) Multiplex color router in a CMOS image sensor. Reproduced with permission.<sup>[79]</sup> Copyright 2017, American Chemical Society. e) (left) See-through meta-lens for cross-polarized ( $\sigma$ ) and co-polarized ( $-\sigma$ ) incident optical waves, (right) full-color augmented reality imaging results. Reproduced with permission.<sup>[178]</sup> Copyright 2018, Springer Nature. f) Folded compact spectrometer. Reproduced with permission.<sup>[179]</sup> Copyright 2018, Springer Nature. g) High-dimensional quantum light source by meta-lens array. Reproduced with permission.<sup>[181]</sup> Copyright 2020, American Association for the Advancement of Science.

manipulation, etc., by the combination of specific multiple IRUs. The optical properties of various IRUs are collected into a large database of meta-lens nanostructures. The complex nanoantenna array layout of the meta-lens can be generated elegantly and efficiently by artificial intelligence assisted design. Current advanced semiconductor micro- and nano-electronics mass production technology and equipment are well established to produce nanostructured meta-lenses with feasible sizes for novel applications.

The applications of meta-lens in endoscopy, light-field optical imaging, virtual and augmented reality, high-dimensional quantum entanglement optical chip, etc. demonstrate its tremendous potential for future applications such as, machine vision for mini-drones, autonomous vehicles, and artificial intelligence robots for agriculture, biomedical, healthcare, and quantum information technologies. We believe that the

artificial nanostructures used for the manipulation of electrons will also work extensively for the control of the photons, giving rise to a new era of optical meta-devices (optical metachips).

## Acknowledgements

The authors acknowledge financial support from the National Key R&D Program of China (2017YFA0303700), the National Natural Science Foundation of China (11774163), and the Shenzhen Science and Technology Innovation Commission under Grant No. SGDX2019081623281169. They are also grateful for the funding support to the State Key Laboratories in Hong Kong from the Innovation and Technology Commission (ITC) of the Government of the Hong Kong Special Administrative Region (HKSAR), China. M.K.C., Y.W., and D.P.T. would also like to express their sincere thanks to the financial support from the Research Office, H.K. PolyU (Project code: BBXE). This article

is part of the *Advanced Optical Materials* Hall of Fame article series, which recognizes the excellent contributions of leading researchers to the field of optical materials science.

## Conflict of Interest

The authors declare no conflict of interest.

## Keywords

meta-devices, meta-lenses, metasurfaces, nanophotonic devices, planar optics

Received: August 19, 2020

Revised: December 12, 2020

Published online: January 12, 2021

- 
- [1] S. L. Sun, K. Y. Yang, C. M. Wang, T. K. Juan, W. T. Chen, C. Y. Liao, Q. He, S. Y. Xiao, W. T. Kung, G. Y. Guo, L. Zhou, D. P. Tsai, *Nano Lett.* **2012**, *12*, 6223.
- [2] W. L. Hsu, P. C. Wu, J. W. Chen, T. Y. Chen, B. H. Cheng, W. T. Chen, Y. W. Huang, C. Y. Liao, G. Sun, D. P. Tsai, *Sci. Rep.* **2015**, *5*, 11226.
- [3] H. C. Wang, C. H. Chu, P. C. Wu, H. H. Hsiao, H. J. Wu, J. W. Chen, W. H. Lee, Y. C. Lai, Y. W. Huang, M. L. Tseng, S. W. Chang, D. P. Tsai, *Small* **2018**, *14*, 1703920.
- [4] Y. W. Huang, W. T. Chen, W. Y. Tsai, P. C. Wu, C. M. Wang, G. Sun, D. P. Tsai, *Nano Lett.* **2015**, *15*, 3122.
- [5] W. T. Chen, K. Y. Yang, C. M. Wang, Y. W. Huang, G. Sun, I. D. Chiang, C. Y. Liao, W. L. Hsu, H. T. Lin, S. Sun, L. Zhou, A. Q. Liu, D. P. Tsai, *Nano Lett.* **2014**, *14*, 225.
- [6] P. C. Wu, J. W. Chen, C. W. Yin, Y. C. Lai, T. L. Chung, C. Y. Liao, B. H. Chen, K. W. Lee, C. J. Chuang, C. M. Wang, D. P. Tsai, *ACS Photonics* **2018**, *5*, 2568.
- [7] P. C. Wu, W. M. Zhu, Z. X. Shen, P. H. J. Chong, W. Ser, D. P. Tsai, A. Q. Liu, *Adv. Opt. Mater.* **2017**, *5*, 1600938.
- [8] P. C. Wu, W. Y. Tsai, W. T. Chen, Y. W. Huang, T. Y. Chen, J. W. Chen, C. Y. Liao, C. H. Chu, G. Sun, D. P. Tsai, *Nano Lett.* **2017**, *17*, 445.
- [9] W. T. Chen, P. Torok, M. R. Foreman, C. Y. Liao, W. Y. Tsai, P. R. Wu, D. P. Tsai, *Nanotechnology* **2016**, *27*, 224002.
- [10] W. Y. Tsai, T. L. Chung, H. H. Hsiao, J. W. Chen, R. J. Lin, P. C. Wu, G. Sun, C. M. Wang, H. Misawa, D. P. Tsai, *Adv. Mater.* **2019**, *31*, 1806479.
- [11] K. C. Shen, Y. T. Huang, T. L. Chung, M. L. Tseng, W. Y. Tsai, G. Sun, D. P. Tsai, *Phys. Rev. Appl.* **2019**, *12*, 064056.
- [12] M. Semmlinger, M. Zhang, M. L. Tseng, T. T. Huang, J. Yang, D. P. Tsai, P. Nordlander, N. J. Halas, *Nano Lett.* **2019**, *19*, 8972.
- [13] M. Semmlinger, M. L. Tseng, J. Yang, M. Zhang, C. Zhang, W. Y. Tsai, D. P. Tsai, P. Nordlander, N. J. Halas, *Nano Lett.* **2018**, *18*, 5738.
- [14] K. C. Shen, C. T. Ku, C. Hsieh, H. C. Kuo, Y. J. Cheng, D. P. Tsai, *Adv. Mater.* **2018**, *30*, 1706918.
- [15] W. Yang, S. Xiao, Q. Song, Y. Liu, Y. Wu, S. Wang, J. Yu, J. Han, D.-P. Tsai, *Nat. Commun.* **2020**, *11*, 1864.
- [16] Y. W. Huang, H. W. H. Lee, R. Sokhoyan, R. A. Pala, K. Thyagarajan, S. Han, D. P. Tsai, H. A. Atwater, *Nano Lett.* **2016**, *16*, 5319.
- [17] C. H. Chu, M. L. Tseng, J. Chen, P. C. Wu, Y. H. Chen, H. C. Wang, T. Y. Chen, W. T. Hsieh, H. J. Wu, G. Sun, D. P. Tsai, *Laser Photonics Rev.* **2016**, *10*, 1600106.
- [18] T. W. Ebbesen, H. J. Lezec, H. F. Ghaemi, T. Thio, P. Wolff, *Nature* **1998**, *391*, 667.
- [19] S. A. Maier, *Plasmonics: Fundamentals and Applications*, Springer, New York **2007**.
- [20] X. G. Luo, D. P. Tsai, M. Gu, M. H. Hong, *Adv. Opt. Photonics* **2018**, *10*, 757.
- [21] S. Ishii, A. V. Kildishev, V. M. Shalaev, K.-P. Chen, V. P. Drachev, *Opt. Lett.* **2011**, *4*, 451.
- [22] S. Jia, X. Wang, Y. Wu, M. X, P. Fan, Z. Wang, *Appl. Phys. Express* **2015**, *8*, 062001.
- [23] Y. Gao, J. Liu, X. Zhang, Y. Wang, Y. Song, S. Liu, Y. Zhang, *Opt. Express* **2012**, *2*, 1320.
- [24] Z. Sun, H. K. Kim, *Appl. Phys. Lett.* **2004**, *85*, 642.
- [25] H. Shi, C. Wang, C. Du, X. Luo, X. Dong, H. Gao, *Opt. Express* **2005**, *13*, 6815.
- [26] T. Xu, C. Wang, C. Du, X. Luo, *Opt. Express* **2008**, *16*, 4753.
- [27] L. Verslegers, P. B. Catrysse, Z. Yu, J. S. White, E. S. Barnard, M. L. Brongersma, S. Fan, *Nano Lett.* **2009**, *9*, 235.
- [28] L. Verslegers, P. B. Catrysse, Z. Yu, S. Fan, *Phys. Rev. Lett.* **2009**, *103*, 033902.
- [29] M. A. Kats, N. Yu, P. Genevet, Z. Gaburro, F. Capasso, *Opt. Express* **2011**, *19*, 21748.
- [30] J. D. Jackson, *Classical Electrodynamics*, 3rd ed, Wiley, New York **1998**.
- [31] N. Yu, P. Genevet, M. A. Kats, F. Aieta, J.-P. Tetienne, F. Capasso, Z. Gaburro, *Science* **2011**, *334*, 333.
- [32] N. Yu, F. Aieta, P. Genevet, M. A. Kats, Z. Gaburro, F. Capasso, *Nano Lett.* **2012**, *12*, 6328.
- [33] P. Genevet, N. Yu, F. Aieta, J. Lin, M. A. Kats, R. Blanchard, M. O. Scully, Z. Gaburro, F. Capasso, *Appl. Phys. Lett.* **2012**, *100*, 013101.
- [34] A. V. Kildishev, A. Boltasseva, V. M. Shalaev, *Science* **2013**, *339*, 1232009.
- [35] N. Yu, F. Capasso, *Nat. Mater.* **2014**, *13*, 139.
- [36] F. Aieta, P. Genevet, M. A. Kats, N. Yu, R. Blanchard, Z. Gaburro, F. Capasso, *Nano Lett.* **2012**, *12*, 4932.
- [37] X. Ni, S. Ishii, A. V. Kildishev, V. M. Shalaev, *Light Sci. Appl.* **2013**, *2*, e72.
- [38] L. Huang, X. Chen, H. Mühlenbernd, G. Li, B. Bai, Q. Tan, G. Jin, T. Zentgraf, S. Zhang, *Nano Lett.* **2012**, *12*, 5750.
- [39] L. Huang, X. Chen, H. Mühlenbernd, H. Zhang, S. Chen, B. Bai, Q. Tan, G. Jin, K.-W. Cheah, C.-W. Qiu, J. Li, T. Zentgraf, S. Zhang, *Nat. Commun.* **2013**, *4*, 2808.
- [40] X. Yin, Z. Ye, J. Rho, Y. Wang, X. Zhang, *Science* **2013**, *339*, 1405.
- [41] X. Li, L. Chen, Y. Li, X. Zhang, M. Pu, Z. Zhao, X. Ma, Y. Wang, M. Hong, X. Luo, *Sci. Adv.* **2016**, *2*, e1601102.
- [42] M. Kang, T. Feng, H.-T. Wang, J. Li, *Opt. Express* **2012**, *20*, 15882.
- [43] X. Chen, L. Huang, H. Mühlenbernd, G. Li, B. Bai, Q. Tan, G. Jin, C.-W. Qiu, S. Zhang, T. Zentgraf, *Nat. Commun.* **2012**, *3*, 1198.
- [44] Z. Bornzon, G. Biener, V. Kleiner, E. Hasman, *Opt. Lett.* **2002**, *27*, 1141.
- [45] E. Hasman, V. Kleiner, G. Biener, A. Niv, *Appl. Phys. Lett.* **2003**, *82*, 328.
- [46] A. Niv, G. Biener, V. Kleiner, E. Hasman, *Opt. Lett.* **2004**, *29*, 238.
- [47] S. Sun, Q. He, S. Xiao, Q. Xu, X. Li, L. Zhou, *Nat. Mater.* **2012**, *11*, 426.
- [48] W. Ma, D. Jia, X. Yu, Y. Feng, Y. Zhao, *Appl. Phys. Lett.* **2016**, *108*, 071111.
- [49] A. Pors, M. G. Nielsen, R. L. Eriksen, S. I. Bozhevolnyi, *Nano Lett.* **2013**, *13*, 829.
- [50] S. Zhang, M.-H. Kim, F. Aieta, A. She, T. Mansuripur, I. Gabay, M. Khorasaninejad, D. Rousso, X. Wang, M. Troccoli, N. Yu, F. Capasso, *Opt. Express* **2016**, *24*, 18024.
- [51] M. Pu, X. Li, X. Ma, Y. Wang, Z. Zhao, C. Wang, C. Hu, P. Gao, C. Huang, H. Ren, X. Li, F. Qin, J. Yang, M. Gu, M. Hong, X. Luo, *Sci. Adv.* **2015**, *1*, e1500396.
- [52] Y. Guo, X. Ma, M. Pu, X. Li, Z. Zhao, X. Luo, *Adv. Opt. Mater.* **2018**, *6*, 1800592.
- [53] C. Pfeiffer, A. Grbic, *Phys. Rev. Lett.* **2013**, *110*, 197401.
- [54] C. Pfeiffer, N. K. Emani, A. M. Shaltout, A. Boltasseva, V. M. Shalaev, A. Grbic, *Nano Lett.* **2014**, *14*, 2491.

- [55] M. Decker, I. Staude, M. Falkner, J. Dominguez, D. N. Neshev, I. Brener, T. Pertsch, Y. S. Kivshar, *Adv. Opt. Mater.* **2015**, *3*, 813.
- [56] L. Zhang, J. Ding, H. Zheng, S. An, H. Lin, B. Zheng, Q. Du, G. Yin, J. Michon, Y. Zhang, Z. Fang, M. Y. Shalaginov, L. Deng, T. Gu, Hu. Zhang, J. Hu, *Nat. Commun.* **2018**, *9*, 1481.
- [57] Y. F. Yu, A. Y. Zhu, R. Paniagua-Domínguez, Y. H. Fu, B. Luk'yanchuk, A. I. Kuznetsov, *Laser Photonics Rev.* **2015**, *9*, 412.
- [58] A. Arbabi, Y. Horie, M. Bagheri, A. Faraon, *Nat. Nanotechnol.* **2015**, *10*, 937.
- [59] S. Vo, D. Fattal, W. V. Sorin, Z. Peng, T. Tran, M. Fiorentino, R. G. Beausoleil, *IEEE Photonics Technol. Lett.* **2014**, *26*, 1375.
- [60] A. Arbabi, R. M. Briggs, Y. Horie, M. Bagheri, A. Faraon, *Opt. Express* **2015**, *23*, 33310.
- [61] A. Zhan, S. Colburn, R. Trivedi, T. K. Fryett, C. M. Dodson, A. Majumdar, *ACS Photonics* **2016**, *3*, 209.
- [62] S. Kruk, B. Hopkins, I. I. Kravchenko, A. Miroshnichenko, D. N. Neshev, Y. S. Kivshar, *APL Photonics* **2016**, *1*, 030801.
- [63] R. Paniagua-Domínguez, Y. F. Yu, E. Khaidarov, S. Choi, V. Leong, R. M. Bakker, X. Liang, Y. H. Fu, V. Valuckas, L. A. Krivitsky, A. I. Kuznetsov, *Nano Lett.* **2018**, *18*, 2124.
- [64] S. Astilean, P. Lalanne, P. Chavel, E. Cambriil, H. Launois, *Opt. Lett.* **1998**, *23*, 552.
- [65] P. Lalanne, S. Astilean, P. Chavel, E. Cambriil, H. Launois, *Opt. Lett.* **1998**, *23*, 1081.
- [66] P. Lalanne, *J. Opt. Soc. Am. A* **1999**, *16*, 2517.
- [67] P. Lalanne, S. Astilean, P. Chavel, E. Cambriil, H. Launois, *J. Opt. Soc. Am. A* **1999**, *16*, 1143.
- [68] A. Arbabi, Y. Horie, A. J. Ball, M. Bagheri, A. Faraon, *Nat. Commun.* **2015**, *6*, 7069.
- [69] M. Khorasaninejad, A. Y. Zhu, C. Roques-Carmes, W. T. Chen, J. Oh, I. Mishra, R. C. Devlin, F. Capasso, *Nano Lett.* **2016**, *16*, 7229.
- [70] D. Lin, P. Fan, E. Hasman, M. L. Brongersma, *Science* **2014**, *345*, 298.
- [71] F. Lu, F. G. Sedgwick, V. Karagodsky, C. Chase, C. J. Chang-Hasnain, *Opt. Express* **2010**, *18*, 12606.
- [72] D. Fattal, J. Li, Z. Peng, M. Fiorentino, R. G. Beausoleil, *Nat. Photonics* **2010**, *4*, 466.
- [73] P. R. West, J. L. Stewart, A. V. Kildishev, V. M. Shalae, V. V. Shkunov, F. Strohkendl, Y. A. Zakharenkov, R. K. Dodds, R. Byren, *Opt. Express* **2014**, *22*, 26212.
- [74] M. Khorasaninejad, K. B. Crozier, *Nat. Commun.* **2014**, *5*, 5386.
- [75] H. Zuo, D.-Y. Choi, X. Gai, P. Ma, L. Xu, D. N. Neshev, B. Zhang, B. Luther-Davies, *Adv. Opt. Mater.* **2017**, *5*, 1700585.
- [76] Q. Fan, M. Liu, C. Yang, L. Yu, F. Yan, T. Xu, *Appl. Phys. Lett.* **2018**, *113*, 201104.
- [77] Q. Fan, Y. Wang, M. Liu, T. Xu, *Opt. Lett.* **2018**, *43*, 6005.
- [78] M. Khorasaninejad, W. T. Chen, R. C. Devlin, J. Oh, A. Y. Zhu, F. Capasso, *Science* **2016**, *352*, 1190.
- [79] B. H. Chen, P. C. Wu, V.-C. Su, Y.-C. Lai, C. H. Chu, I. C. Lee, J.-W. Chen, Y. H. Chen, Y.-C. Lan, C.-H. Kuan, D. P. Tsai, *Nano Lett.* **2017**, *17*, 6345.
- [80] M. Khorasaninejad, W. T. Chen, A. Y. Zhu, J. Oh, R. C. Devlin, D. Rousso, F. Capasso, *Nano Lett.* **2016**, *16*, 4595.
- [81] B. Groever, N. A. Rubin, J. P. B. Mueller, R. C. Devlin, F. Capasso, *Sci. Rep.* **2018**, *8*, 7240.
- [82] S. Zhang, A. Soibel, S. A. Keo, D. Wilson, S. B. Rafol, D. Z. Ting, A. She, S. D. Gunapala, F. Capasso, *Appl. Phys. Lett.* **2018**, *113*, 111104.
- [83] W. T. Chen, A. Y. Zhu, M. Khorasaninejad, Z. Shi, V. Sanjeev, F. Capasso, *Nano Lett.* **2017**, *17*, 3188.
- [84] H. Liang, Q. Lin, X. Xie, Q. Sun, Y. Wang, L. Zhou, L. Liu, X. Yu, J. Zhou, T. F. Krauss, J. Li, *Nano Lett.* **2018**, *18*, 4460.
- [85] A. B. Klemm, D. Stellinga, E. R. Martins, L. Lewis, G. Huyet, L. O'Faolain, T. F. Krauss, *Opt. Lett.* **2013**, *38*, 3410.
- [86] Z.-B. Fan, Z.-K. Shao, M.-Y. Xie, X.-N. Pang, W.-S. Ruan, F.-L. Zhao, Y.-J. Chen, S.-Y. Yu, J.-W. Dong, *Phys. Rev. Appl.* **2018**, *10*, 014005.
- [87] A. Arbabi, E. Kamali, S. M. Horie, Y. Han, S. Han, A. Faraon, *Nat. Commun.* **2016**, *7*, 13682.
- [88] R. Kingslake, *A history of the Photographic Lens*, Elsevier, New York **1989**.
- [89] B. Groever, W. T. Chen, F. Capasso, *Nano Lett.* **2017**, *17*, 4902.
- [90] F. Aieta, M. A. Kats, P. Genevet, F. Capasso, *Science* **2015**, *347*, 1342.
- [91] Z. Zhao, M. Pu, H. Gao, J. Jin, X. Li, X. Ma, Y. Wang, P. Gao, X. Luo, *Sci. Rep.* **2015**, *5*, 15781.
- [92] E. Arbabi, A. Arbabi, S. M. Kamali, Y. Horie, A. Faraon, *Optica* **2016**, *3*, 628.
- [93] E. Arbabi, A. Arbabi, S. M. Kamali, Y. Horie, A. Faraon, *Sci. Rep.* **2016**, *6*, 32803.
- [94] O. Avayu, E. Almeida, Y. Prior, T. Ellenbogen, *Nat. Commun.* **2017**, *8*, 14992.
- [95] M. Khorasaninejad, Z. Shi, A. Y. Zhu, W. T. Chen, V. Sanjeev, A. Zaidi, F. Capasso, *Nano Lett.* **2017**, *17*, 1819.
- [96] E. Arbabi, A. Arbabi, S. M. Kamali, Y. Horie, A. Faraon, *Optica* **2017**, *4*, 625.
- [97] H. H. Hsiao, Y. H. Chen, R. J. Lin, P. C. Wu, S. M. Wang, B. H. Chen, D. P. Tsai, *Adv. Opt. Mater.* **2018**, *6*, 1800031.
- [98] S. M. Wang, P. C. Wu, V.-C. Su, Y.-C. Lai, C. H. Chu, J.-W. Chen, S.-H. Lu, J. Chen, B. B. Xu, C.-H. Kuan, T. Li, S. N. Zhu, D. P. Tsai, *Nat. Commun.* **2017**, *8*, 187.
- [99] S. Wang, P. C. Wu, V.-C. Su, Y.-C. Lai, M.-K. Chen, H. Y. Kuo, B. H. Chen, Y. H. Chen, T.-T. Huang, J.-H. Wang, R.-M. Lin, C.-H. Kuan, T. Li, Z. Wang, S. Zhu, D. P. Tsai, *Nat. Nanotechnol.* **2018**, *13*, 227.
- [100] Q. Q. Cheng, M. L. Ma, D. Yu, Z. X. Shen, J. Y. Xie, J. C. Wang, N. X. Xu, H. M. Guo, W. Hu, S. M. Wang, T. Li, S. L. Zhuang, *Sci. Bull.* **2019**, *64*, 1525.
- [101] W. T. Chen, A. Y. Zhu, V. Sanjeev, M. Khorasaninejad, Z. Shi, E. Lee, F. Capasso, *Nat. Nanotechnol.* **2018**, *13*, 220.
- [102] W. T. Chen, A. Y. Zhu, J. Sisler, Y.-W. Huang, K. M. A. Yousef, E. Lee, C.-W. Qiu, F. Capasso, *Nano Lett.* **2018**, *18*, 7801.
- [103] S. Shrestha, A. C. Overvig, M. Lu, A. Stein, N. Yu, *Light Sci. Appl.* **2018**, *7*, 85.
- [104] W. T. Chen, A. Y. Zhu, J. Sisler, Z. Bharwani, F. Capasso, *Nat. Commun.* **2019**, *10*, 335.
- [105] P. Gutruf, C. Zou, W. Withayachumnankul, M. Bhaskaran, S. Sriram, C. Fumeaux, *ACS Nano* **2016**, *10*, 133.
- [106] N. I. Zheludev, Y. S. Kivshar, *Nat. Mater.* **2012**, *11*, 917.
- [107] S. Song, X. Ma, M. Pu, X. Li, K. Liu, P. Gao, Z. Zhao, Y. Wang, C. Wang, X. Luo, *Adv. Opt. Mater.* **2017**, *5*, 1600829.
- [108] H.-S. Ee, R. Agarwal, *Nano Lett.* **2016**, *16*, 2818.
- [109] S. M. Kamali, E. Arbabi, A. Arbabi, Y. Horie, A. Faraon, *Laser Photonics Rev.* **2016**, *10*, 1002.
- [110] F. Cheng, L. Qiu, D. Nikolov, A. Bauer, J. P. Rolland, A. N. Vamivakas, *Opt. Express* **2019**, *27*, 15194.
- [111] A. O'Halloran, F. O'Malley, P. McHugh, *J. Appl. Phys.* **2008**, *104*, 71101.
- [112] A. She, S. Zhang, S. Shian, D. R. Clarke, F. Capasso, *Sci. Adv.* **2018**, *4*, eaap9957.
- [113] P. Brochu, Q. Pei, *Macromol. Rapid Commun.* **2010**, *31*, 10.
- [114] J. Huang, T. Li, C. C. F. J. Zhu, D. R. Clarke, Z. Suo, *Appl. Phys. Lett.* **2012**, *100*, 41911.
- [115] S. J. A. Koh, T. Li, J. Zhou, X. Zhao, W. Hong, J. Zhu, Z. Suo, *J. Polym. Sci. Part B Polym. Phys.* **2011**, *49*, 504.
- [116] W. M. Zhu, Q. H. Song, L. B. Yan, W. Zhang, P.-C. Wu, L. K. Chin, H. Cai, D. P. Tsai, Z. X. Shen, T. W. Deng, S. K. Ting, Y. D. Gu, G. Q. Lo, D. L. Kwong, Z. C. Yang, R. Huang, A.-Q. Liu, N. Zheludev, *Adv. Mater.* **2015**, *27*, 4739.
- [117] Q. Wang, E. T. F. Rogers, B. Gholipour, C.-M. Wang, G. Yuan, J. Teng, N. I. Zheludev, *Nat. Photonics* **2015**, *10*, 60.
- [118] Y. Chen, X. Li, Y. Sonnefraud, A. I. Fernández-Domínguez, X. Luo, M. Hong, S. A. Maier, *Sci. Rep.* **2015**, *5*, 8660.

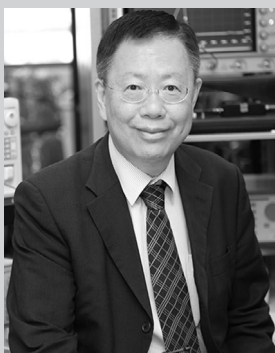
- [119] W. Bai, P. Yang, S. Wang, J. Huang, D. Chen, Z. Zhang, J. Yang, B. Xu, *Nanomaterials* **2019**, *9*, 993.
- [120] S. Li, C. Zhou, G. Ban, H. Wang, H. Lu, Y. Wang, *J. Phys. D: Appl. Phys.* **2019**, *52*, 095106.
- [121] Z. D. Huang, B. Hu, W. G. Liu, J. Liu, Y. T. Wang, *J. Opt. Soc. Am. B* **2017**, *34*, 1848.
- [122] P. Ding, Y. Li, L. Shao, X. Tian, J. Wang, C. Fan, *Opt. Express* **2018**, *26*, 28038.
- [123] Z. Yin, Q. Zheng, K. Wang, K. Guo, F. Shen, H. Zhou, Y. Sun, Q. Zhou, J. Gao, L. Luo, Z. Guo, *Opt. Commun.* **2018**, 429, 41.
- [124] T.-T. Kim, H. Kim, M. Kenney, H. S. Park, H.-D. Kim, B. Min, S. Zhang, *Adv. Opt. Mater.* **2018**, *6*, 1700507.
- [125] W. G. Liu, B. Hu, Z. D. Huang, H. Y. Guan, H. T. Li, X. K. Wang, Y. Zhang, H. X. Yin, X. L. Xiong, J. Liu, Y. T. Wang, *Photonics Res.* **2018**, *6*, 703.
- [126] Z. Zhang, X. Yan, L. J. Liang, D. Q. Wei, M. Wang, Y. R. Wang, J. Q. Yao, *Carbon* **2018**, *132*, 529.
- [127] P. Berto, L. Philippet, J. Osmond, C. F. Liu, A. Afridi, M. M. Marques, B. M. Agudo, G. Tessier, R. Quidant, *Nat. Photonics* **2019**, *13*, 649.
- [128] A. Afridi, J. Canet-Ferrer, L. Philippet, J. Osmond, P. Berto, R. Quidant, *ACS Photonics* **2018**, *5*, 4497.
- [129] G. Zheng, W. Wu, Z. Li, S. Zhang, M. Q. Mehmood, P. He, S. Li, *Opt. Lett.* **2017**, *42*, 1261.
- [130] H. Markovich, D. S. Filonov, I. I. Shishkin, P. Ginzburg, *IEEE Trans. Antennas Propag.* **2018**, *66*, 2650.
- [131] H. Markovich, I. I. Shishkin, N. Hendler, P. Ginzburg, *Nano Lett.* **2018**, *18*, 5024.
- [132] R. Fu, Z. Li, G. Zheng, M. Chen, Y. Yang, J. Tao, L. Wu, Q. Deng, *Opt. Express* **2019**, *27*, 12221.
- [133] M. D. Aiello, A. S. Backer, A. J. Sapon, J. Smits, J. D. Perreault, P. Llull, V. M. Acosta, *ACS Photonics* **2019**, *6*, 2432.
- [134] J. W. Zhong, N. An, N. B. Yi, M. X. Zhu, Q. H. Song, S. M. Xiao, *Plasmonics* **2016**, *11*, 537.
- [135] C.-Y. Fan, T.-J. Chuang, K.-H. Wu, G.-D. J. Su, *Opt. Express* **2020**, *28*, 10609.
- [136] O. Solgaard, *Photonic Microsystems: Micro and Nanotechnology Applied to Optical Devices and Systems*, Springer, New York **2009**.
- [137] T. Roy, S. Zhang, I. W. Jung, M. Troccoli, F. Capasso, D. Lopez, *APL Photonics* **2018**, *3*, 021302.
- [138] E. Arbabi, A. Arbabi, S. M. Kamali, Y. Horie, M. Faraji-Dana, A. Faraon, *Nat. Commun.* **2018**, *9*, 812.
- [139] I. Shimoyama, *IEEE/RISJ Intell. Robots Syst.* **1995**, *2*, 208.
- [140] R. S. Fearing, *IEEE/RISJ Intell. Robots Syst.* **1995**, *2*, 212.
- [141] A. Zhan, S. Colburn, C. M. Dodson, A. Majumdar, *Sci. Rep.* **2017**, *7*, 1673.
- [142] E. R. Dowski, W. T. Cathey, *Appl. Opt.* **1995**, *34*, 1859.
- [143] S. Bradburn, W. T. Cathey, E. R. Dowski, *Appl. Opt.* **1997**, *36*, 9157.
- [144] L. W. Alvarez, *US patent, US 3305294 A*, **1967**.
- [145] S. Barbero, *Opt. Express* **2009**, *17*, 9376.
- [146] S. Colburn, A. Zhan, A. Majumdar, *Optica* **2018**, *5*, 825.
- [147] C. Hong, S. Colburn, A. Majumdar, *Appl. Opt.* **2017**, *56*, 8822.
- [148] D. Lin, M. Melli, E. Poliakov, P. S. Hilaire, S. Dhuey, C. Peroz, S. Cabrini, M. Brongersma, M. Klug, *Sci. Rep.* **2017**, *7*, 2286.
- [149] S. Bernet, M. Ritsch-Marte, *Appl. Opt.* **2008**, *47*, 3722.
- [150] Z. Jaroszewicz, A. Kolodziejczyk, A. Mira, R. Henao, S. Bará, *Opt. Express* **2005**, *13*, 918.
- [151] Y. Cui, G. Zheng, M. Chen, Y. Zhang, Y. Yang, J. Tao, T. He, Z. Li, *Chin. Opt. Lett.* **2019**, *17*, 111603.
- [152] N. Yilmaz, A. Ozdemir, A. Ozer, H. Kurt, *J. Opt.* **2019**, *21*, 045105.
- [153] Y. Guo, M. Pu, X. Ma, X. Li, R. Shi, X. Luo, *Appl. Phys. Lett.* **2019**, *15*, 163103.
- [154] X. Luo, *Engineering Optics 2.0*, Springer, New York **2019**, p. 531.
- [155] J. P. B. Mueller, N. A. Rubin, R. C. Devlin, B. Groever, F. Capasso, *Phys. Rev. Lett.* **2017**, *118*, 113901.
- [156] R. C. Devlin, A. Ambrosio, N. A. Rubin, J. P. B. Mueller, F. Capasso, *Science* **2017**, *358*, 896.
- [157] Q. B. Fan, W. Q. Zhu, Y. Z. Liang, P. C. Huo, C. Zhang, A. Agrawal, K. Huang, X. G. Luo, Y. Q. Lu, C. W. Qiu, H. J. Lezec, T. Xu, *Nano Lett.* **2018**, *19*, 1158.
- [158] E. Arbabi, S. M. Kamal, A. Arbabi, A. Faraon, *ACS Photonics* **2018**, *5*, 3132.
- [159] Z. Yang, Z. Wang, Y. Wang, X. Feng, M. Zhao, Z. Wan, L. Zhu, J. Liu, Y. Huang, J. Xia, M. Wegener, *Nat. Commun.* **2018**, *9*, 4607.
- [160] N. A. Rubin, G. D. Aversa, P. Chevalier, Z. Shi, W. Chen, F. Capasso, *Science* **2019**, *43*, 365.
- [161] C. Yan, X. Li, M. Pu, X. Ma, F. Zhang, P. Gao, K. Liu, X. Luo, *Appl. Phys. Lett.* **2019**, *114*, 161904.
- [162] J. Bai, C. Wang, X. Chen, A. Barisi, C. Wang, Y. Yao, *Photonics Res.* **2019**, *7*, 1051.
- [163] J. Zhou, H. Qian, C. Chen, J. Zhao, G. Li, Q. Wu, H. Luo, S. Wen, Z. Liu, *Proc. Natl. Acad. Sci. USA* **2019**, *23*, 11137.
- [164] Y. Zhou, H. Zheng, I. I. Kravchenko, J. Valentine, *Nat. Photonics* **2020**, *14*, 316.
- [165] P. Huo, C. Zhang, W. Zhu, M. Liu, Song. Zhang, Si. Zhang, L. Chen, H. J. Lezec, A. Agrawal, Y. Lu, T. Xu, *Nano Lett.* **2020**, *20*, 2791.
- [166] H. Kwon, E. Arbabi, S. M. Kamali, M. Faraji-Dana, A. Faraon, *Nat. Photonics* **2019**, *14*, 109.
- [167] R. J. Lin, V. C. Su, S. Wang, M. K. Chen, T. L. Chung, Y. H. Chen, H. Y. Kuo, J. W. Chen, J. Chen, Y. T. Huang, J. H. Wang, C. H. Chu, P. C. Wu, T. Li, Z. Wang, S. Zhu, D. P. Tsai, *Nat. Nanotechnol.* **2019**, *14*, 227.
- [168] M. K. Chen, C. H. Chu, R. J. Lin, J. W. Chen, Y. T. Huang, T. T. Huang, H. Y. Kuo, D. P. Tsai, *Jpn. J. Appl. Phys.* **2019**, *58*, SK0801.
- [169] Z. Fan, H. Qiu, H. Zhang, X. Pang, L. Zhou, L. Liu, H. Ren, Q. Wang, J. Dong, *Light Sci. Appl.* **2019**, *8*, 67.
- [170] Q. Guo, Z. Shi, Y. Huang, E. Alexander, C. Qiu, F. Capasso, T. Zickler, *Proc. Natl. Acad. Sci. USA* **2019**, *46*, 22959.
- [171] A. L. Holsteen, D. Lin, I. Kauvar, G. Wetzstein, M. L. Brongersma, *Nano Lett.* **2019**, *19*, 2267.
- [172] V.-C. Su, C. H. Chu, G. Sun, D. P. Tsai, *Opt. Express* **2018**, *26*, 13148.
- [173] M. L. Tseng, H.-H. Hsiao, C. H. Chu, M. K. Chen, G. Sun, A.-Q. Li, D. P. Tsai, *Adv. Opt. Mater.* **2018**, *6*, 1800554.
- [174] H.-H. Hsiao, C. H. Chu, D. P. Tsai, *Small Methods* **2017**, *1*, 1600064.
- [175] H. Pahlevaninezhad, M. Khorasaninejad, Y. W. Huang, Z. Shi, L. P. Hariri, D. C. Adams, V. Ding, A. Zhu, C.-W. Qiu, F. Capasso, M. J. Suter, *Nat. Photonics* **2018**, *12*, 540.
- [176] C. Chen, W. Song, J. Chen, J. Wang, Y. Chen, B. Xu, M. Chen, H. Li, B. Fang, J. Chen, H. Kuo, S. Wang, D. P. Tsai, S. Zhu, T. Li, *Light Sci. Appl.* **2019**, *8*, 99.
- [177] E. Arbabi, J. Li, R. J. Hutchins, S. M. Kamali, A. Arbabi, Y. Horie, P. V. Dorpe, V. Gradinaru, D. A. Wagenaar, A. Faraon, *Nano Lett.* **2018**, *18*, 4943.
- [178] G. Lee, J. Hong, S. Hwang, S. Moon, H. Kang, S. Jeon, H. Kim, J. Jeong, B. Lee, *Nat. Commun.* **2018**, *9*, 4562.
- [179] M. Faraji-Dana, E. Arbabi, A. Arbabi, S. M. Kamali, H. Kwon, A. Faraon, *Nat. Commun.* **2018**, *9*, 4196.
- [180] C. Schlickriede, N. Waterman, B. Reineke, P. Gorgi, G. Li, S. Zhang, Thomas. Zentgraf, *Adv. Mater.* **2018**, *30*, 1703843.
- [181] L. Li, Z. X. Liu, X. F. Ren, S. M. Wang, V.-C. Su, M.-K. Chen, C. H. Chu, H. Y. Kuo, B. H. Liu, W. B. Zang, G. C. Guo, L. J. Zhang, Z. L. Wang, S. N. Zhu, D. P. Tsai, *Science* **2020**, *368*, 1487.
- [182] W. Li, J. Qi, A. Sihvola, *Adv. Opt. Mater.* **2020**, *8*, 2001000.



**Mu Ku Chen** received his Ph.D. degree from the Department of Physics and Institute of Applied Physics of the National Taiwan University in 2019. He was a postdoctoral research fellow, and is currently a research assistant professor at the Department of Electronic and Information Engineering, The Hong Kong Polytechnic University. His research interests include photonic information, nanophotonics, micro- and nanoelectronics fabrication, and artificial nanoantenna array-based meta-devices for photonic applications.



**Ting Xu** received his joint Ph.D. degree from the Chinese Academy of Sciences and University of Michigan in 2011. He is now a professor at the National Laboratory of Solid-State Microstructures, College of Engineering and Applied Science, Nanjing University, China. He directs an optics laboratory, and his research interests include photonic metamaterials, metasurfaces, and meta-devices.



**Din Ping Tsai** received his Ph.D. degree from the University of Cincinnati, USA in 1990. Currently, he is the Head and chair professor of the Department of Electronic and Information Engineering, The Hong Kong Polytechnic University. He is a Fellow of AAAS, APS, EMA, IEEE, NAI, OSA, and SPIE. His current research interests are nanostructured semiconductor electronic and photonic meta-devices and systems for emerging electronics and high-dimensional quantum optical information applications.